

1 **Distinctive aerosol-cloud-precipitation interactions in marine boundary layer clouds from the**
2 **ACE-ENA and SOCRATES aircraft field campaigns**

3
4 Xiaojian Zheng^{1,a}, Xiquan Dong¹, Baike Xi¹, Timothy Logan² and Yuan Wang³

5
6 ¹Department of Hydrology and Atmospheric Sciences, University of Arizona, Tucson, AZ, USA

7 ²Department of Atmospheric Sciences, Texas A&M University, College Station, TX, USA

8 ³Department of Earth System Sciences, Stanford University, Stanford, CA, USA

9 ^aNow at: Environmental Science Division, Argonne National Laboratory, Lemont, IL, USA

10
11 **Correspondence:** Xiquan Dong (xdong@arizona.edu)

12
13 **Abstract.** The aerosol-cloud-precipitation interactions within the cloud-topped Marine Boundary Layer
14 (MBL), are being examined using aircraft in-situ measurements from Aerosol and Cloud Experiments in
15 the Eastern North Atlantic (ACE-ENA) and Southern Ocean Clouds Radiation Aerosol Transport
16 Experimental Study (SOCRATES) field campaigns. SOCRATES clouds have a larger number (148.3
17 cm^{-3}) and smaller cloud droplets ($8.0 \mu\text{m}$) compared to ACE-ENA summertime (89.4 cm^{-3} and $9.0 \mu\text{m}$)
18 and wintertime clouds (70.6 cm^{-3} and $9.8 \mu\text{m}$). The ACE-ENA clouds, especially in wintertime, exhibit
19 stronger drizzle formation and growth due to enhanced collision-coalescence, attributed to the relatively
20 cleaner environment and deeper cloud layer. Furthermore, the Aerosol-Cloud Interaction (ACI) indices
21 from the two aircraft field campaigns suggest distinct sensitivities, indicating the cloud microphysical
22 responses to aerosols reside in different regimes. Aerosols during ACE-ENA winter are more likely to
23 be activated into cloud droplets under sufficient water availability and strong turbulence, given the
24 aerosol-limited regime. The enriched aerosol loading during ACE-ENA summer and SOCRATES
25 generally leads to smaller cloud droplets competing for available water vapor and exhibiting a stronger

26 ACI in the water-vapor-limit regime. Notably, the precipitation susceptibilities are more pronounced
27 during the ACE-ENA than during the SOCRATES campaigns. The in-cloud drizzle evolutions
28 significantly alter sub-cloud cloud condensation nuclei (CCN) budgets through the coalescence-
29 scavenging effect, and in turn, impact the ACI assessments. The results of this study can enhance the
30 understanding and aid in future model simulation and assessment of the aerosol-cloud interaction.

31

32

33 **1. Introduction**

34 Marine boundary layer (MBL) clouds substantially impact the Earth's climate system (Dong and
35 Minnis, 2022). Sustained by large-scale subsidence and cloud-top longwave radiative cooling, MBL
36 clouds, typically located beneath the temperature inversion at the MBL top, persistently reflect the
37 incoming solar radiation and modulate the radiative balance (Lilly, 1968; Albrecht et al., 1995; Wood et
38 al., 2015; Dong et al., 2023). The climatic significance of MBL cloud radiative effects, which remains
39 largely uncertain (IPCC, 2022), is closely linked to cloud microphysical properties that are substantially
40 influenced by surrounding aerosol conditions (Chen et al., 2014; Feingold and McComiskey, 2016).
41 Observational evidence demonstrates that cloud microphysical responses to aerosols, defined as the
42 aerosol-cloud interaction (ACI), can be typically viewed as decreased cloud droplet effective radii (r_c)
43 and increased number concentrations (N_c) with more aerosol intrusion, under conditions of comparable
44 cloud water content (Feingold and McComiskey, 2016). The ACIs have been extensively investigated
45 by different observational platforms, such as aircraft (Hill et al., 2009; Diamond et al., 2018; Gupta et
46 al., 2022), ground-based and satellite observations (Painemal et al., 2020; Zhang et al., 2022; Zheng et
47 al., 2022a), and model simulations (Wang et al., 2020; Christensen et al., 2023) over different maritime
48 regions like the southeast Pacific (Painemal and Zuidema, 2011), northeast Pacific (Braun et al., 2018),
49 southeast Atlantic (Gupta et al., 2022), and eastern North Atlantic (Zheng et al., 2022a)..

50 Furthermore, more and smaller cloud droplets not only extend cloud longevity and spatial
51 coverage but also modulate the precipitation processes, reflecting the cloud adjustments to aerosol
52 disturbances (Albrecht, 1989; Bellouin et al., 2020). Precipitation, particularly in the form of drizzle, is
53 common in MBL clouds (Wood et al., 2015; Wu et al., 2020), and the turbulence forced by stratocumulus
54 cloud-top radiative cooling can increase the cloud liquid water path, and contribute to drizzle production
55 (Ghate et al., 2019, 2021). The drizzle formation and growth processes are deeply entwined with the
56 MBL aerosols and dynamics. Aerosols have been found to suppress the precipitation frequency and
57 strength by constantly buffering cloud droplet number concentrations via activation, hence increasing
58 cloud precipitation susceptibility (Feingold and Seibert, 2009; Lu et al., 2009; Sorooshian et al., 2009;
59 Duong et al., 2011). Furthermore, the assessments of precipitation susceptibility are examined to be under
60 the influences of methodology (Terai et al., 2012), cloud morphology (Sorooshian et al., 2009; Jung et
61 al., 2016), ambient aerosol concentrations (Duong et al., 2011; Jung et al., 2016; Gupta et al., 2022), and
62 cloud thickness (Terai et al., 2012; Jung et al., 2016; Gupta et al., 2022). The in-cloud turbulence and
63 wind shear can effectively enhance collision-coalescence efficiency, stimulating drizzle formation and
64 growth, and consequently leading to enhanced precipitation (Chen et al., 2011; Wu et al., 2017). Cloud-
65 top entrainment of dryer and warmer air can potentially deplete small cloud droplets and shrink large
66 droplets via evaporation, thereby impacting cloud top microphysical processes depending on the
67 homogeneous or inhomogeneous mixing regimes (Lehmann et al., 2009; Jia et al., 2019).

68 Conversely, precipitation has been shown to exert a substantial influence on the MBL aerosol and
69 cloud condensation nuclei (CCN) budget through the coalescence-scavenging effect. The coalescence-
70 scavenging refers to the process in which cloud or drizzle droplets, containing aerosol particles, merge
71 with each other. Upon the collision-coalescence of cloud droplets, the dissolved aerosol masses within
72 the cloud droplets also collide and merge into a larger aerosol core, leading to larger aerosol particles
73 upon droplet evaporation. The sub-cloud aerosols are then replenished into the cloud layer, experiencing
74 growth within the cloud through cloud and drizzle droplet collision-coalescence, and subsequently falling

75 and evaporating outside the cloud again. Eventually, the residual aerosols undergoing this cloud-
76 processing cycle will gradually decrease in number concentration and increase in size (Flossmann et al.,
77 1985; Feingold et al., 1996; Hudson and Noble, 2020; Hoffmann and Feingold, 2023). In addition, the
78 drizzle drops, once falling out of the cloud base, can result in net reductions in sub-cloud aerosols and
79 CCN budgets also via the precipitation scavenging processes (Wood, 2006; Zheng et al., 2022b).
80 Quantitative estimates of these effects remain ambiguous and inconclusive, which are subject to multiple
81 factors such as aerosol physicochemical characteristics, cloud morphology, and MBL dynamics and
82 thermodynamics conditions (Sorooshian et al., 2009; Duong et al., 2011; Diamond et al., 2018; Brunke
83 et al., 2022). Thus, more studies on the aforementioned processes regarding MBL aerosols and clouds
84 over different maritime regions are warranted to pursue an in-depth understanding of aerosol-cloud-
85 precipitation interactions (ACPIs).

86 The Eastern North Atlantic (ENA) stands as a desirable region for exploring MBL clouds in the
87 mid-latitude, with Graciosa Island in the Azores (39.09°N, 28.03°W) representing a focal point for such
88 studies. Located between the mid-latitude and subtropical climate zones, Graciosa is subject to the
89 meteorological influence of both the Icelandic Low and the Azores High, and the influence of aerosols
90 ranging from pristine marine air masses to those heavily influenced by continental emissions from North
91 America and Northern Europe (Logan et al., 2014; Wood et al., 2015; Wang et al., 2020). Addressing
92 the need for sustained research into the MBL clouds, the recent Aerosol and Cloud Experiments in the
93 Eastern North Atlantic (ACE-ENA) aircraft campaign (J. Wang et al., 2022) were conducted in the
94 summer (June and July) 2017 (ACEENA Sum) and winter (January and February) 2018 (ACEENA Win).
95 During these two intensive operation periods (IOPs) of ACE-ENA, the research aircraft accrued abundant
96 in-situ measurements of aerosols, clouds, and drizzle properties, providing invaluable resources for
97 studying the ACI and ACPI processes. During the summer, the Azores is located at the eastern part of
98 the high-pressure system, while during the winter, the center of the Azores high shifts to the eastern
99 Atlantic and is primarily located directly over the Azores (Mechem et al., 2018; J. Wang et al., 2022).

100 Furthermore, both summer and winter IOPs of ACE-ENA are featured with anomalous stronger high-
101 pressure systems, compared to the 20-year climatology as shown in Figure S1. This meteorological
102 pattern is favorable to the prevailing and persistent stratocumulus clouds observed during the ACE-ENA,
103 especially for the winter IOP, where the enhanced large-scale subsidence would lead to a deeper
104 stratocumulus-topped MBL (Rémillard and Tselioudis, 2015; Jensen et al., 2021). The ACE-ENA
105 summer IOP is characterized by anomalously low MBL heights and substantial MBL decoupling (Miller
106 et al., 2021; J. Wang et al., 2022), while the winter IOP is featured with prevalent precipitation-generated
107 cold pools, where evaporative cooling alters the thermodynamical structure of the MBL, sustains and
108 enhances turbulence mixing, hence contributes to dynamical perturbations that can influence the behavior
109 of the MBL (Terai and Wood, 2013; Zuidema et al., 2017; Jensen et al., 2021; J. Wang et al., 2022).
110 Over the recent years, many observational studies, based on the ACE-ENA data, have focused on the
111 seasonal contrasts of the aerosol distributions and sources (Y. Wang et al., 2021b; Zawadowicz et al.,
112 2021), the cloud and drizzle microphysics vertical distributions (Wu et al., 2020a; Zheng et al., 2022b),
113 as well as the impacts of MBL conditions on the cloud structure and morphology (Jensen et al., 2021).
114 However, they seldom analyze the comprehensive interactions between aerosol, clouds and precipitation.

115 Over the Southern Ocean (SO), the Southern Ocean Clouds Radiation Aerosol Transport
116 Experimental Study (SOCRATES) field campaign (McFarquhar et al., 2021) was conducted during the
117 austral summer (January and February 2018), which marks another valuable piece of the MBL cloud
118 research. The SO, being one of the cloudiest regions globally, is predominantly influenced by naturally
119 produced aerosols originating from oceanic sources due to its remoteness, where the anthropogenic and
120 biomass burning aerosols exert minimal influence over the region (McCoy et al., 2021; Sanchez et al.,
121 2021; Twohy et al., 2021; Zhang et al., 2023). The aerosol budget in this region is primarily shaped by
122 biological aerosols, which nucleate from the oxidation products of dimethyl sulfide (DMS) emissions, as
123 well as by sea spray aerosols. Hence, the SO provides an unparalleled natural laboratory for discerning
124 the influence of these natural aerosol emissions on the MBL clouds under a pre-industrial natural

125 environment. The summertime SO region, particularly near the SOCRATES focus area, is characterized
126 by more frequently closed-cell mesoscale cellular convection structures (Danker et al., 2022; Lang et al.,
127 2022). Furthermore, the MBL clouds over the SO predominantly consist of supercooled liquid water
128 droplets, which coexist with mixed- and ice-phase processes (Y. Wang et al., 2021a; Xi et al., 2022),
129 while the precipitation phases are examined to be primarily dominated by liquid hydrometeors (Tansey
130 et al., 2022; Kang et al., 2024). The in-situ measurements collected from SOCRATES have cultivated
131 numerous studies on aerosols, clouds, and precipitation over the SO using both in-situ measurements and
132 model simulations (McCoy et al., 2020; Altas et al., 2021; D'Alessandro et al., 2021), and provides an
133 opportunity to study the liquid cloud processes under a colder nature. As shown in Figure S1c,
134 compositely speaking, the SOCRATES cloud cases used in this study are located ahead of the anomaly-
135 stronger thermal ridge and behind the thermal trough, providing a set up favorable to the closed cellular
136 MBL cloud structures (McCoy et al., 2017; Lang et al., 2022). While the region of selected SOCRATES
137 cloud cases crosses a larger latitudinal zone and is under more consistent influence of mid-latitude
138 cyclone systems than over the ACE-ENA region, the cloud sampling periods used in this study majority
139 reside in the closed-cell MBL stratocumulus decks.

140 The cloud cases selected from the ACE-ENA and SOCRATES share similar cloud morphology
141 (stratocumulus) while experiencing different aerosol sources and meteorological conditions. Using a
142 synergistic approach to compare data from these different field campaigns can provide valuable insights
143 to the community regarding the functioning physical processes of the interactions between aerosols,
144 clouds, and precipitation under the influence of different MBL dynamic and thermodynamic conditions.
145 This study targets the similarities and differences in the MBL aerosol, cloud, and drizzle properties, their
146 distribution and evolution, and more appealingly, the ACIs and ACPIs between the two campaigns. The
147 data and methods used in this study are introduced in section 2. The aerosol and CCN properties in the
148 above- and sub-cloud regimes, as well as the vertical distributions of MBL cloud and drizzle properties,
149 are examined in section 3. The ACI, precipitation susceptibility and drizzle impacts on the sub-cloud

150 aerosols and CCN (ACPI) are discussed in section 4. Finally, the findings are summarized, and the
151 importance of this study is discussed in section 5.

152

153 **2. Data and methods**

154 **2.1 Cloud and drizzle properties**

155 The in-situ measurements of MBL cloud properties are temporally synchronized to 1 Hz
156 resolution, corresponding to approximately 100 m (5 m) of horizontal (vertical) sampling. The sampling
157 locations of the selected cases are indicated by the white dots in Figure S1. The Fast Cloud Droplet Probe
158 (FCDP) onboard the aircraft during ACE-ENA can detect droplets with diameter (D_p) ranging from 1.5
159 μm to 50 μm , with the size bins of the probe between 1 and 3 μm (Glienke and Mei, 2020). While the
160 SOCRATES used a similar CDP to measure droplets from 2 μm to 50 μm at a 2 μm probe size bin width.
161 Both ACE-ENA and SOCRATES leverage the Two-Dimensional Stereo Particle Imaging Probe (2DS)
162 to discern droplets with diameters from 5 μm to 1280 μm (Lawson et al., 2006; Glienke and Mei, 2019).
163 The 2DS in-situ measurements will be used as additional screening to eliminate the ice particles with
164 diameters larger than 200 μm . Moreover, the University of Washington Ice–Liquid Discriminator
165 product, which is a Machine-learning-based single-particle phase classification of the 2DS images (Atlas
166 et al., 2021), is used to identify small ice crystals when available. Through these three datasets, we can
167 tease out the ice-dominated period to the utmost extent and focus on the liquid cloud processes and ACI
168 during the SOCRATES (Wang et al., 2021).

169 Although these in-situ measurements can provide “ground-truth” datasets, their uncertainties
170 must be properly analyzed and data quality must be controlled before being applied to scientific studies.
171 The uncertainties of FCDP in sizing and concentration are approximately 30% and 20%, respectively
172 (Baumgardner et al., 2017). Considering the significant uncertainty in the concentration of smaller
173 particles from a photodiode probe such as 2DS (Baumgardner & Korolev, 1997; Wang et al., 2021), a
174 diameter of 40 μm is used as the demarcation line between cloud droplets and drizzle drops (Wood et al.,

175 2005). Then droplet number concentrations in the overlapping size bin between FCDP and 2DS are
 176 redistributed assuming a gamma distribution, thereby a complete size spectrum of cloud and drizzle can
 177 be merged from FCDP and 2DS measurements. Hence, the cloud and drizzle microphysical properties
 178 can be calculated.

179 The cloud droplet number concentration (N_c) is given by:

$$180 N_c = \int_2^{40} n(D_p) dD_p, \quad (1)$$

181 The cloud droplet effective radius (r_c , Hansen and Travis, 1974) is given by:

$$182 r_c = \frac{\int_2^{40} r_p^3 n(D_p) dD_p}{\int_2^{40} r_p^2 n(D_p) dD_p}, \quad (2)$$

183 The cloud liquid water content (LWC_c) can be calculated by:

$$184 LWC_c = \frac{4}{3} \pi \rho_w \int_2^{40} D^3 n(D_p) dD_p, \quad (3)$$

185 where ρ_w is water density.

186 Similarly, the drizzle drop number concentration (N_d) and liquid water content (LWC_d) can be calculated
 187 using the size distribution from 40 μm to 1280 μm . Particularly, the drizzle mean mass diameter (D_{mmd})
 188 is given by:

$$189 D_{mmd} = \left(\frac{\int_{40}^{1280} D_p^3 n(D_p) dD_p}{\int_{40}^{1280} n(D_p) dD_p} \right)^{1/3}, \quad (4)$$

190 This quantity is chosen because the D_{mmd} denotes the diameter of average mass (the third-moment
 191 average) of the drizzle size distribution, which provides the link between the number concentration and
 192 the mass concentration of drizzle droplets in a sample (Hinds, 1999).

193 Adapting the method in Zheng et al. (2022b), the cloud base precipitation rate (R_{CB}) is given by:

$$194 R_{CB}(mm/hr) = 6\pi * 10^{-4} \int_{40\mu m}^{1280\mu m} D_{p,mm}^3 n(D_{p,mm}) U_{\infty}(D_{p,mm}) dD_{p,mm}, \quad (5)$$

195 in order to match the unit conversion, the $D_{p,mm}$ is diameter in unit of mm, $n(D_{p,mm})$ is drizzle number
196 concentration in every size bin with a unit of $\# \text{ m}^3 \text{ mm}^{-1}$, and $U_{\infty}(D_{p,mm})$ is terminal velocity in given
197 size bin, which is calculated from the full Reynolds number theory as in Pruppacher and Klett (2010).

198 The combined threshold of $N_c > 5 \text{ cm}^{-3}$ and $LWC_c > 0.01 \text{ g m}^{-3}$ is used for determining the valid
199 cloud samples and cloud boundaries (Wood, 2005; Zheng et al., 2022b). The complete cloud vertical
200 profiles from sub-cloud to the above-cloud are selected during the ACE-ENA and SOCRATES IOPs, in
201 which the flight strategy includes sawtooth and spiral cloud transects and ramping cloud sampling. The
202 precipitation conditions are determined by whether samples of $N_d > 0.001 \text{ cm}^{-3}$ exists below the cloud
203 base height. In total, the selected numbers of cloud (precipitating cloud) profiles are 18 (13), 26 (13), and
204 28 (24) for ACE-ENA summer and winter IOPs along with SOCRATES, respectively. The detailed
205 selected cloud profiles are listed in Table S1, along with the cloud profile macrophysics.

206 Furthermore, the assessments of ACI are significantly impacted by the MBL dynamic and
207 thermodynamic conditions. Jones et al. (2011) suggested that the MBL would be in a well-mixed and
208 coupled condition when the difference in liquid water potential temperature (θ_L) and total water mixing
209 ratio (q_t) between the bottom of MBL and the inversion layer are less than 0.5 K and 0.5 g/kg,
210 respectively. In this regard, since the coupled and decoupled MBL conditions coexist in the selected
211 cloud cases in this study, particularly in ACE-ENA summer, which is characterized by anomalously low
212 BL heights and substantial BL decoupling. Previous studies found that, under the decoupling condition,
213 the aerosols, CCN, and moisture sources near the surface are disconnected from the cloud layer aloft,
214 hence exerting much less effective impact on the cloud microphysics (Zheng et al., 2022a; Christensen
215 et al., 2023). Therefore, we adapt and modify the metric in Jones et al. (2011) to calculate the sub-cloud
216 coupled layer, in order to ensure the aerosols and CCN measured sub-cloud are in a well-mixed state and
217 can represent the actual interaction (or contact) with the cloud layer. In this study, the q_t and θ_L at the
218 cloud base are calculated, and then their vertical variations are examined starting from the altitude of

219 cloud base (z_b) and looking downward. As such, the coupled point altitude (z_{cp}) is defined as the altitude
220 where the vertical changes in q_t and θ_L exceed 0.5 K and 0.5 g/kg, respectively. Hence, the coupled layer
221 ($H_{cp} = z_t - z_{cp}$) is defined as the layer between the cloud top altitude (z_t) and coupled point altitude
222 (z_{cp}), hence the selection of the aerosols and CCN within the below-cloud part of the coupled layer can
223 be viewed as in contact with the cloud. An example of the coupled layer identification is shown in Figure
224 S2. Therefore, the degree of MBL decoupling (D_{cp}) can be quantified as the ratio of the coupled sub-
225 cloud MBL thickness to the sub-cloud MBL thickness, where $D_{cp} = 1 - (H_{cp} - H_c)/z_b$. As shown in
226 Table S1, the ACE-ENA summer feature with highest degree of decoupling (averaged $D_{cp}=0.504$),
227 compared to the ACE-ENA winter ($D_{cp}=0.370$) and SOCRATES ($D_{cp}=0.277$).

228

229 **2.2 Aerosol properties**

230 The total aerosol number concentrations (N_a) from ACE-ENA and SOCRATES are measured by
231 the airborne Condensation Particle Counter (CPC) models 3772 and 3760A, which counts the number of
232 aerosols with diameter (D_p) larger than 3 nm and 11 nm, respectively (Kuang and Mei, 2019;
233 SOCRATES Low Rate Data, 2022). Additionally, the Passive Cavity Aerosol Spectrometer (PCASP)
234 onboard the ACE-ENA aircraft is capable of sizing the aerosol with D_p ranging from 0.1 μm to 3.2 μm
235 (Goldberger, 2020). While the ultra-high sensitivity aerosol spectrometer (UHSAS) measures the size-
236 resolved aerosol distribution from 0.06 μm to 1.0 μm during SOCRATES (Uin, 2016). Therefore, the
237 number concentrations of accumulation mode aerosols (N_{ACC} , 0.1 μm -1 μm) can be discerned from the
238 PCASP and UHSAS aerosol size distributions. The Aitken mode aerosols (N_{Ait} , $< 0.1 \mu\text{m}$) from the
239 ACE-ENA is given by the fast integrated mobility spectrometer (FIMS), which can size the aerosol down
240 to 9 nm (Olfert et al., 2008), while the N_{Ait} from SOCRATES is limited to 0.06 μm – 0.1 μm due to the
241 limitation of UHSAS. As for the CCN measurements, the ACE-ENA utilized the Dual-Column CCN
242 Counter at two constant supersaturation levels of 0.15% and 0.35% (Uin and Mei, 2019), while the CCN

243 number concentration (N_{CCN}) during SOCRATES was measured under various supersaturation levels
244 from 0.06% to 0.87% using a scanning CCN counter (Roberts and Nenes, 2005). In this study, N_{CCN} at
245 0.35% supersaturation ($N_{CCN0.35\%}$) is used to ensure a direct comparison between ACE-ENA and
246 SOCRATES. The aerosol measurements are in the temporal resolution of 1Hz. Note that the aerosol and
247 CCN data are quality-controlled by removing the data point where the $N_c + N_d$ greater than 5 cm^{-3} or N_d
248 greater than 0.01 cm^{-3} , to filter out the contamination of the cloud droplets, and drizzle water splashing.

249 The sub-cloud aerosols and CCN are selected within the below cloud base part of the coupled
250 layer, which is described in last section, in order to better assess the aerosol-cloud interactions. The
251 above-cloud aerosols and CCN are selected between the cloud top and 200 m above. Note that the
252 selection criteria of 200 m above the cloud top would inevitably induce uncertainty in the cloud top ACI
253 assessment, depending on the vertical trend of the individual aerosol profile. Over the Southeast Atlantic,
254 Gupta et al. (2021) conducted an analysis focusing particularly on the differing impacts when biomass
255 burning aerosols are in contact with marine stratocumulus cloud tops, using 100 m above as the
256 demarcation, versus when they are separated by various distances, and found that significant differences
257 were observed in cloud microphysics, owing to different droplet evaporation and nucleation, compared
258 to separated profiles. That result is in agreement with the modeling sensitivity study over the Eastern
259 North Atlantic by Wang et al. (2020), who found that aerosol plumes can exert impacts on the cloud-top
260 microphysics only when they are in close contact with the cloud layer. In most cases, the ACE-ENA
261 feature is a rather stable or slightly decreasing profile within a couple hundred meters above the cloud
262 top, while the long-range transports, particularly during summertime, will induce an elevated aerosol
263 layer in higher altitudes that is not in contact with the cloud layer. While the frequent new particle
264 formation events during SOCRATES will significantly alter the free-troposphere Aitken mode aerosol
265 budget, they would need to further subside down to impact the cloud (McCoy et al., 2021; Zhang et al.,
266 2023). Therefore, the 200 m criteria used in this study are in the reconciliation of getting the close-to-
267 cloud aerosol plumes and enough sample size for statistical analysis.

268

269

270 **3. Aerosol, cloud, and drizzle properties of selected cases**

271 **3.1 Aerosols and CCN in above- and sub-cloud regimes**

272 The probability density functions (PDFs) of aerosols, CCN, and cloud microphysical properties
273 from selected cases during the ACE-ENA and SOCRATES field campaigns are presented in Figure 1.
274 Notably, the N_a , N_{Acc} and $N_{CCN0.35\%}$ values from the SOCRATES are the highest among the three IOPs,
275 followed by the ACE-ENA summer and winter as illustrated in both above-cloud (Figs. 1a-1c) and sub-
276 cloud regimes (Figs. 1d-1f). Such variations can be linked to the disparate aerosol sources in the ACE-
277 ENA and SOCRATES regions, especially during the summer and winter seasons over the Azores.

278 In the SOCRATES region, according to the previous studies involving back-trajectory analyses,
279 dominant air masses within the MBL primarily originate from the south or from the west, skirting the
280 Antarctic coast (Zhang et al., 2023), while the air masses above the MBL follow a similar transport
281 pathway, they can also originate from the tip of southern Africa and transport southeast along the warm
282 conveyor belt (McCoy et al., 2021). The SOCRATES above-cloud aerosols (674.6 cm⁻³) are primarily
283 constituted by the Aitken mode aerosols because the mean N_{Acc} is only 62.5 cm⁻³. Previously, McCoy
284 et al. (2021) reported average values of 680.69 cm⁻³, 546.28 cm⁻³ and 465.05 cm⁻³ for mid-troposphere,
285 above and below cloud for the multiple SOCRATES cases, respectively. While for the individual cases
286 the above cloud aerosols vary from a couple hundred to over a thousand (McCoy et al., 2021; Zhang et
287 al., 2023). These aerosols are predominantly produced from the oxidation of biogenic gases, notably the
288 dimethyl sulfide (DMS) emitted by marine biological productivity (Sanchez et al., 2018; McCoy et al.,
289 2020). The rising air currents in MBL transport these particles into the free troposphere (FT) with
290 dominant aerosol population over the SO (McCoy et al., 2021; Sanchez et al., 2021). And hence, it
291 reinforces the notion that the SO represents a pre-industrial marine environment where the influence of
292 anthropogenic and biomass-burning aerosols is mostly negligible (McCoy et al., 2020, 2021).

293 Conversely, the ENA region experiences aerosols of varied origins, spanning maritime air masses
294 to those heavily influenced by continental emissions from North America or Northern Europe, especially
295 during the summertime (Logan et al., 2014; Wang et al., 2020). The summertime air mass back-
296 trajectories within the MBL strongly feature recirculating flow around the Azores high. During the
297 wintertime, however, the air masses predominantly originate in the FT, are transported above the MBL,
298 and are then further entrained down to the MBL by large-scale subsidence, indicating less influence from
299 continental pollution (Y. Wang et al., 2021b). During the summer ACE-ENA campaign, the MBL is
300 enriched by sulfate and carbonaceous particles (Y. Wang et al., 2021b; Zawadowicz et al., 2021). This
301 enhancement is attributed both to local generation from DMS and to the long-range transport from the
302 continental air masses, resulting in the mean N_a of 312.6 cm⁻³ and 301.5 cm⁻³ for above- and sub-cloud
303 regimes, respectively. The ACE-ENA winter exhibits the lowest aerosol and CCN concentrations,
304 predominantly sourced from local maritime influences, and coupled with reduced continental air mass
305 intrusions (Zheng et al., 2018; Y. Wang et al., 2021b).

306 Figure 1a reveals that there are more above-cloud N_a during the three IOPs than sub-cloud values,
307 especially during the SOCRATES. The higher above-cloud N_a values from the three IOPs are primarily
308 contributed by Aitken mode aerosols because their corresponding N_{Acc} values are much lower (Figs.
309 1a&b). It is interesting to note that the above-cloud $N_{CCN0.35\%}$ values exceed the N_{Acc} for all three IOPs
310 (Figs. 1b&c), implying that a significant fraction of Aitken mode aerosols can be activated to become
311 CCN, corroborating findings from earlier studies (McCoy et al., 2021; Zheng et al., 2021). For the sub-
312 cloud regime, the N_a values during SOCRATES and ACE-ENA winter are ~70-80% of their
313 corresponding above-cloud values, and the N_a during ACE-ENA summer is almost identical to its above-
314 cloud value. Notice that the sub-cloud N_{Acc} values from three IOPs are more than double of the above-
315 cloud N_{Acc} values, and most of the sub-cloud accumulation mode aerosol can be activated to become
316 CCN at SS of 0.35%. It is interesting to note that the higher $N_{CCN0.35\%}$ at sub-cloud layer during

317 SOCRATES may partially result from the cloud process on aerosols (Figs. 1e&f), which is suggested by
318 previous studies (McCoy et al., 2021; Zhang et al., 2023), and will be further discussed in Section 3.1.

319 To further investigate the above- and sub-cloud aerosol properties from three IOPs, the aerosol
320 droplet size distributions are analyzed in Figure 2. It is evident that SOCRATES aerosols have the highest
321 concentrations of Aitken mode particles ($D_p = 0.06 - 0.1 \mu\text{m}$, given that the $< 0.06 \mu\text{m}$ is not available
322 from UHSAS) for both the above- and sub-cloud regimes. McCoy et al. (2021) and Zheng et al. (2021)
323 identified analogous origins and formations of the above-cloud Aitken mode aerosols over both the SO
324 and ENA regions and concluded that these aerosols primarily originate from the nucleation of photo-
325 oxidation products of DMS, notably H_2SO_4 and MSA, in the free troposphere (FT). The differential
326 concentrations can be ascribed to the fact that sea-surface DMS concentrations in the SO are generally
327 higher than those in the ENA region (Aumont et al., 2002; Zhang et al., 2023). Moreover, DMS emissions
328 in the ENA during summer surpass those during winter (Zawadowicz et al., 2021). For the accumulation
329 mode aerosols ($0.1 - 1 \mu\text{m}$), the N_{Acc} values for both above- and sub-cloud regimes during SOCRATES
330 decrease monotonically with particle size. The results in Figure 2 further support the finding that Aitken
331 mode aerosols are dominant over the SO. The N_{Acc} values during ACE-ENA show slight uplifts for the
332 small accumulation mode aerosols ($< 0.3 \mu\text{m}$), particularly for summer, reflecting the signal of potential
333 long-range transport of fine-mode aerosols (Wang et al., 2020; Y. Wang et al., 2021b). Consequently,
334 such comparison reinforces the notion that the SO represents a largely pre-industrial marine environment,
335 wherein the influence of anthropogenic and biomass-burning aerosols is minimal (McCoy et al., 2020,
336 2021; Zhang et al., 2023).

337 When contrasting the aerosol size distributions in the sub-cloud regime (Fig. 2b) with those in the
338 above-cloud regime, the influence of cloud processing on aerosols is discernibly non-trivial, particularly
339 under the cloud-topped MBL conditions examined in this study. While the FT aerosols can be further
340 entrained down and contribute to the population of Aitken mode aerosols within the MBL, the sub-cloud

341 aerosols can also be subject to the influence of new particle formation in the upper MBL, though arguably
342 less effective than those within the FT (Zheng et al., 2021). Additionally, in-cloud Brownian capture can
343 lead to a substantial reduction in Aitken mode aerosols (Hudson et al., 2015; Wyant et al., 2022),
344 providing the rationale for the observed decrease in Aitken mode aerosols in the sub-cloud regime,
345 especially for particles smaller than 0.07 μm . In addition, cloud chemical processing, such as the
346 aqueous-phase condensation of sulfuric acid onto the aerosol cores inside the cloud droplets, is
347 particularly pronounced during the transitioning of Aitken mode aerosols to accumulation mode aerosols
348 (Hudson et al., 2015; Zhang et al., 2023).

349 From both above- to sub-cloud regimes, the larger Aitken mode aerosols ($> 0.07 \mu\text{m}$) can be
350 effectively enlarged to accumulation mode aerosols through coagulation and water vapor diffusional
351 growth (Covert et al., 1996), contributing to the elevated accumulation mode aerosol distribution and
352 increased N_{Acc} in the sub-cloud regime. These processes are particularly evidenced by the decrease of
353 critical supersaturations from above-cloud (between 0.35% - 0.4%) to sub-cloud (between 0.3% - 0.35%)
354 during SOCRATES (Fig. S3) because the aerosol droplet sizes are enlarged and more readily become
355 CCN. Furthermore, the collision-coalescence combines mixtures of large and small cloud droplets, and
356 results in the sub-cloud aerosol residuals shifting towards the larger size, upon the droplet evaporation
357 below the cloud (often manifested as drizzle). This partially elucidates the observed increase in the tail-
358 end of the accumulation mode aerosol distribution for all three IOPs. The elevation in sub-cloud coarse
359 mode aerosols observed for both ACE-ENA IOPs (as seen in Fig. 2) can be attributed both to the
360 coalescence-enlargement process and the intrusion of sea spray aerosols (e.g., sea salt). As illustrated
361 and analyzed based on a case study during summertime that exhibits the signal of cloud-processing
362 aerosols (Zheng et al., 2022b), as well as the long-term aerosol physicochemical properties over the
363 ARM-ENA ground-based observatory (Zheng et al., 2018), particularly during the winter season where
364 the production of sea spray aerosol is prevalent.

365

366 3.2 Bulk cloud microphysical properties distribution

367 The PDFs of MBL cloud microphysical properties (N_c , r_c , LWC_c) derived from aircraft in-situ
368 measurements from the three IOPs are shown in Figures 1g-1i. The mean microphysical properties for
369 the individual cloud profiles are listed in Table S2. The results in Figure 1 have demonstrated that
370 aerosol/CCN sources and concentrations, especially from the sub-cloud regime, play an important role
371 in cloud droplet formation and evolution. For example, the SOCRATES has the highest sub-cloud
372 aerosols and CCN, and subsequently feature a larger number of smaller cloud droplets, given the highest
373 N_c (148.3 cm^{-3}) and smallest r_c ($8 \text{ }\mu\text{m}$) among the three IOPs. These results have further confirmed and
374 reassured our understanding of the aerosol first indirect effect: more aerosols induce more smaller cloud
375 droplets (higher N_c and smaller r_c) under constrained liquid water content conditions, thus the MBL
376 clouds reflect more incoming solar radiation (Twomey, 1977). The ACE-ENA wintertime clouds feature
377 the fewest N_c (70.6 cm^{-3}) and largest r_c ($9.8 \text{ }\mu\text{m}$), while the N_c and r_c (89.4 cm^{-3} and $9 \text{ }\mu\text{m}$) during ACE-
378 ENA summer fall between the SOCRATES and ACE-ENA winter values. Considering the aerosol
379 competing effect against the available water vapor, the relatively abundant aerosols in SOCRATES might
380 account for the narrower r_c distribution, which peaks between $6 - 10 \text{ }\mu\text{m}$. SOCRATES has a lower cloud-
381 layer water vapor mixing ratio (figure not shown) compared to ACE-ENA because the SO region has
382 been observed to contain less precipitable water vapor than the ENA region due to the colder sea surface
383 temperatures (Marcovecchio et al., 2023). Therefore, the aerosol and cloud properties in Figure 1 promise
384 further examination of different cloud microphysical responses to aerosols via the ACI process. Note that
385 the $N_{CCN0.35\%}$ and N_c values are lower than N_c values during the ACE-ENA winter IOP, which is also
386 confirmed in previous studies (J. Wang et al., 2022; Wang et al., 2023), which is also confirmed in
387 previous studies (J. Wang et al., 2022; Wang et al., 2023). This interesting phenomenon can potentially
388 be attributed to a combination of factors including lower MBL aerosol sources, stronger in-cloud
389 coalescence-scavenging depletion of sub-cloud aerosols, and the aircraft snapshots capturing the

390 equilibrium states of aerosols and cloud due to enhanced aerosol activations induced by stronger updrafts
391 during the ACE-ENA winter (J. Wang et al., 2022). This thereby compels further investigation into the
392 potential impacts of precipitation on the MBL CCN budget. These aerosol-cloud-precipitation
393 interactions (ACPIs) will be discussed in Section 4.

394

395 **3.3 Vertical distributions of cloud and drizzle microphysics**

396 The vertical distributions of the cloud and drizzle microphysical properties within the cloud layer
397 from the three IOPs are shown in Figure 3. To ensure the representativeness of the vertical profiles, all
398 the in-cloud samples are vertically smoothed by using a triangular moving average method, and are
399 inverse distance weighted in every 50 m moving altitude windows. Furthermore, the altitude is then
400 normalized by $z_i = \frac{z - z_{base}}{z_{top} - z_{base}}$, where $z_i = 0$ denotes cloud base and $z_i = 1$ denotes cloud top.

401 Consistent with previous discussions on the bulk microphysics distribution, the mean N_c values from
402 SOCRATES are consistently higher than ACE-ENA summer and winter for the entire cloud layer, with
403 a slight increase ranging from the cloud base to the upper-middle part ($z_i \approx 0.85$) and then decreasing
404 toward the cloud top due to cloud-top entrainment (Fig. 3a). All r_c values from the three IOPs show a
405 near-linear increase from cloud base to top, with the smallest values observed during SOCRATES and
406 the largest values observed during ACE-ENA winter (Fig. 3b).

407 The warmer and drier air near the cloud top entrains into the cloud layer and further mixes
408 downward, often resulting in the evaporation of small cloud droplets and the shrinking of droplet sizes,
409 which oppose condensational growth (Desai et al., 2021). Decreases in both N_c and LWC_c , and the
410 reduced growth of r_c near the cloud top ($z_i > 0.85$) support signals of cloud-top entrainment mixing
411 during all three IOPs. It is interesting to note that the r_c values from SOCRATES increase monotonically
412 from cloud base to top, while the r_c values from both ACE-ENA summer and winter increase until $z_i \approx$
413 0.8 and then remain nearly constant, although all of their N_c values (at $z_i \approx 0.8$) decrease towards the

414 cloud top. When dry air entrainment occurs at the cloud top, some of the upper-level smaller cloud
415 droplets will evaporate, which leads to decreases in N_c (Fig. 3a). As cloud-top entrainment mixing can
416 shrink large cloud droplets via evaporation, depending on the entrainment mixing rate, the nearly
417 constant r_c values (at $z_i > 0.8$) might represent the equilibrium balance between two competing
418 processes: cloud droplet condensational and collision-coalescence growths, and the entrainment mixing
419 evaporation effects.

420 While carrying the distinct discrepancies in the mean values for all layers, the N_c and r_c from
421 ACE-ENA summer and winter clouds experienced similar vertical evolutions as the SOCRATES. The
422 increases of r_c (Δr_c) from cloud base to cloud top are 4.03 μm , 4.78 μm and 5.85 μm , with percentage
423 increases of 66%, 68% and 79%, for SOCRATES, ACE-ENA summer and winter, respectively. Even
424 though, theoretically, the condensational growth effect would be more pronounced on smaller cloud
425 droplets due to their smaller surface area (Wallace and Hobbs, 2006), SOCRATES exhibits the thickest
426 mean cloud thickness but experienced the least r_c increases among the three IOPs. This suggests that
427 high aerosol loadings are limiting the overall growth of the cloud DSD in SOCRATES clouds, while the
428 ACE-ENA winter clouds show the strongest r_c increase, in contrast. This comparison suggests different
429 cloud microphysical responses to aerosol perturbations in the three IOPs, which will be further discussed
430 in Section 4.1. The LWC_c values from the three IOPs are comparable to each other. The vertical
431 distributions of MBL cloud microphysical properties examined in this study are in good agreement with
432 the previous studies conducted on these two field campaigns (Wu et al., 2020a; Y. Wang et al., 2021a; J.
433 Wang et al., 2021; Wang et al., 2023). In addition, the cloud adiabaticity is defined as $f_{ad} =$
434 LWC_c/LWC_{ad} , where the LWC_{ad} denotes adiabatic LWC (Wu et al., 2020b). As shown in Figure S4,
435 the clouds from all three IOPs feature certain levels of sub-adiabaticity above the cloud base. Considering
436 the inter-cloud layer-mean f_{ad} , the campaign-mean f_{ad} values are 0.689 ± 0.229 , 0.542 ± 0.143 , and
437 0.490 ± 0.207 for SOCRATES, ACE-ENA summer and winter, respectively. It has been well known that

438 cloud sub-adiabaticity is primarily induced by the in-cloud collision-coalescence and the entrainment
439 mixing processes (Hill et al., 2009; Braun et al., 2018; Gao et al., 2020; Wu et al., 2020b).

440 To quantitatively evaluate the impact of cloud-top entrainment mixing rate on cloud droplets, we
441 adapt the method of Albrecht et al. (2016), where the cloud-top entrainment rate (w_e) can be expressed
442 as

$$443 \quad w_e = A_\sigma * \sigma_w / R_{i\sigma} , \quad (6)$$

444 where the turbulence kinetic energy (TKE) dissipation coefficient A_σ is empirically taken as 26 as in
445 Albrecht et al. (2016), and the $R_{i\sigma}$ is the buoyancy Richardson number calculated by $(g/\theta_0) * (\Delta\theta_v h / \sigma_w^2)$. σ_w denotes the standard deviation of vertical velocities taken near the cloud top ($z_i > 0.9$),
446 and h is the MBL height. θ_0 is the reference potential temperature and $\Delta\theta_v$ is the virtual potential
447 temperature difference across the temperature inversion layer above the cloud. Given the valid cloud top
448 virtual potential temperature and vertical velocity measurements for the selected cloud cases, the
449 averaged w_e values are $0.570 \pm 0.834 \text{ cm s}^{-1}$, $0.581 \pm 0.560 \text{ cm s}^{-1}$, and $0.960 \pm 1.127 \text{ cm s}^{-1}$ for SOCRATES,
450 ACE-ENA summer and winter, respectively. The stronger w_e during ACE-ENA winter might be induced
451 by the generally weaker cloud-top inversions and stronger near-cloud top turbulence, compared to the
452 summertime when the ENA is dominated by the large-scale high-pressure system (Ghate et al., 2021).
453 Considering the near cloud-top proportion of cloud where the LWC_c experienced decrease, the difference
454 in LWC_c (between the cloud top value the upper-middle cloud maximum for the mean profiles) for the
455 ACE-ENA summer (-0.032 g m^{-3}) is higher than the reductions in winter (-0.018 g m^{-3}) and SOCRATES
456 (-0.009 g m^{-3}), albeit that the w_e for ACE-ENA summer is comparable to SOCRATES, and much lower
457 than ACE-ENA winter values. Within the above-cloud inversion layer, the temperature (water vapor
458 mixing ratio) differences ΔT (Δq) are 1.76 K (-1.75 g kg^{-1}), 1.54 K (-1.66 g kg^{-1}) and 1.48 K (-1.09 g kg^{-1})
459 for SOCRATES, ACE-ENA summer and winter, respectively. Therefore, the warmer and dryer
460 entrained air can partially contribute to the greater LWC_c reduction and the lower f_{ad} (0.39) during the
461

462 ACE-ENA summer than those during the ACE-ENA winter ($f_{ad} = 0.45$) and SOCRATES ($f_{ad} = 0.66$)
463 near the cloud top (Fig. S4). For the three IOPs, the N_c and LWC_c exhibited a stable trend from the cloud
464 base, followed by a noticeable decrease near the cloud top mixing zone, while the changes in r_c trend
465 were not as dramatic as the others. Such characteristics of the cloud microphysics vertical profiles
466 indicate the signal of inhomogeneous mixing, which occurs when dry and warm air mixes unevenly and
467 not rapidly with the cloud air, hence partially evaporating the cloud droplets (Lehmann et al., 2009; Lu
468 et al., 2011). The results are consistent with findings in stratocumulus clouds over multiple field
469 campaigns (Brenguier et al., 2011; Jia et al., 2019) and with the findings for selected cases during the
470 ACE-ENA (Yeom et al., 2021), and the SOCRATES (Sanchez et al., 2020). While the near-cloud r_c
471 profiles for the ACE-ENA cases exhibit more constant variation, which could be possibly attributed to
472 more effective mixing due to the stronger entrainment rate, particularly during the ACE-ENA winter,
473 eventually reaching a smaller equilibrium in terms of mean sizes.

474 Figures 3d-3f illustrate the normalized profiles of MBL drizzle microphysical properties. The N_d
475 values from the three IOPs mimic each other, which all maximize at the cloud top and then monotonically
476 decrease toward the cloud base (Fig. 3d), while their LWC_d values follow a similar trend, albeit with
477 relatively large differences (Fig. 3f). In contrast to the N_d and LWC_d trends, the D_{mmd} gradually increase
478 from cloud top to cloud base (Fig. 3e), making physical sense since the drizzle droplets are typically
479 formed near cloud top and continuously grow via collision-coalescence process while falling. The ACE-
480 ENA wintertime drizzle D_{mmd} and LWC_d are distinctively larger than those in summertime and
481 SOCRATES. It is interesting to note that near the cloud top ($z_i > 0.9$), the ACE-ENA winter has
482 comparable N_d but much larger D_{mmd} than the other two IOPs, suggesting that there were more large
483 drizzle embryos formed from large cloud droplets (Fig. 3b) during ACE-ENA winter. It is noteworthy
484 that the D_{mmd} in the lower-half region of the ACE-ENA winter clouds experienced rapid growth from

485 ~80 μm to ~105 μm (Fig. 3e), and this increment of ~25 μm contributed to most of the D_{mmd} growth
486 from cloud top to cloud base (33.5 μm), indicating a stronger warm-rain process during the winter.

487 In order to further analyze the cloud-to-drizzle conversion processes, the cloud and drizzle droplet
488 size distributions (DSD) are categorized into four segments based on their relative position within the
489 cloud layer (Fig. 4): upper cloud ($z_i > 0.8$, Fig. 4a), upper-middle cloud ($0.5 \leq z_i < 0.8$, Fig. 4b), lower-
490 middle cloud ($0.2 \leq z_i < 0.5$, Fig. 4c) and lower cloud ($z_i < 0.2$, Fig. 4d). The cloud DSDs ($D_p < 40$
491 μm) from the three IOPs gradually shift towards larger sizes, moving from the lower to the upper cloud
492 regions. This is accompanied by the narrowing of the DSD ranges, as evidenced by the decline in the
493 cloud relative dispersion (ϵ). The relative dispersion of cloud droplets (ϵ) is a parameter that represents
494 the DSD and is defined as the ratio between the standard deviation and the mean radius of the distribution.
495 At the lower portion of the cloud (Fig. 4d), the relatively greater value of ϵ clearly represents the co-
496 existence of the newly formed small cloud droplets from recently activated CCNs and the sedimentation
497 of larger droplets from the upper sections of the cloud. In addition, the discrepancies in ϵ between the
498 three IOPs may be attributed to the sub-cloud aerosol differences, which essentially resided in different
499 microphysical regimes. Y. Wang et al. (2021a) stated that higher aerosol loading would lead to increased
500 ϵ due to the water vapor competition effect, supporting the discrepancy between SOCRATES and ACE-
501 ENA summer IOPs, which can be categorized as a water-vapor-limited regime. Meanwhile, the ACE-
502 ENA wintertime IOP exhibits characteristics of an aerosol-limited regime, in which the cloud DSDs tend
503 to be narrower than in the water-limited regime, due to enhanced droplet growth, and the ϵ values further
504 decrease with height via the condensational narrowing effect (J. Chen et al., 2018).

505 Notably, the cloud DSDs during ACE-ENA winter exhibit a more pronounced negative skew (to
506 the left) than those during ACE-ENA summer, which can be partially attribute to the activation of more
507 sub-cloud coarse mode aerosols to become larger cloud embryos, as demonstrated in Fig. 2. These coarse
508 mode aerosols, whether from primary production of sea spray or from the residuals of evaporated drizzle

509 drops, are more easily activated (or re-activated) into larger cloud droplets when they intrude (or
510 recirculate) into the cloud layer (Hudson and Noble, 2020; Hoffmann and Feingold, 2023). Nevertheless,
511 it is challenging to pinpoint the actual origins of coarse mode aerosols from the perspective of aircraft
512 observational snapshots, thus requiring further numerical modeling work. For the four cloud portions
513 from cloud base to cloud top, the skewness of summertime (wintertime) cloud DSDs are 0.627 (0.271),
514 0.358 (0.175), 0.098 (-0.063), and -0.362 (-0.554), respectively. Ascending within the cloud, the process
515 of water vapor condensation perpetually pushes the DSD towards larger sizes, culminating in a more
516 negatively skewed DSD. Concurrently, the cloud-top entrainment mixing plays a pivotal role in
517 minimizing ε in the upper cloud region, as elaborated by Lu et al. (2023). Note that in the upper region
518 of the cloud (Fig. 4a), the ACE-ENA winter clouds contain more cloud droplets close to 40 μm , albeit
519 the mean N_c is lower. This scenario is conducive to the formation of larger drizzle embryos compared to
520 summertime clouds, as depicted in Fig. 3e. In comparison, the SOCRATES clouds feature a pronounced
521 log-normal DSD than the ACE-ENA, as the DSDs peak at $D_p \sim 15 \mu\text{m}$ throughout the cloud, and
522 subsequently, the lack of larger cloud droplets resulted in the smaller drizzle embryos near the cloud top.
523 As the newly formed drizzle drops descend and continuously grow through the collision-coalescence
524 process, the drizzle DSDs ($D_p > 40 \mu\text{m}$) are noticeably broadened. From upper to lower cloud regions,
525 the longer tails of the drizzle DSDs expand at the cost of smaller drizzle drops and cloud droplets via the
526 collision-coalescence process. The clouds observed during ACE-ENA, especially in wintertime, contain
527 more large drizzle drops ($D_p > 200 \mu\text{m}$) than SOCRATES, which is reflected in the distinct differences
528 in the vertical D_{mmd} as shown in Fig. 3e.

529 It has been intensively studied that in-cloud turbulence can stimulate collision-coalescence and
530 consequently enhance the drizzle evolution processes (Pinsky et al., 2007; Grabowski and Wang, 2013;
531 Wu et al., 2017; S. Chen et al., 2018). The turbulence strength is characterized by the turbulence kinetic
532 energy (TKE), which is calculated as:

533 $TKE = \frac{1}{2}(\overline{u'^2} + \overline{v'^2} + \overline{w'^2})$, (7)

534 where the turbulent perturbations of vertical ($\overline{w'^2}$) and horizontal ($\overline{u'^2}$ and $\overline{v'^2}$) components are
535 calculated as the simple moving variance in a 10s window centered at the measurement time, without
536 window weighting function, using 1Hz data for all three IOPs. The w data is confined to an absolute
537 aircraft roll angle of less than 5° (Cooper et al., 2016). Given the average aircraft ground speed of ~ 140
538 m/s and vertical speed of ~ 5 m/s (Altas et al., 2020), the smallest resolved wavelength is 140 m. Hence,
539 within the 10s moving window, the ~ 50 m in the integral vertical range is able to resolve the eddies up
540 to ~ 1400 m in size, and preserve the potential of capturing the inertial subrange.

541 As shown in Figure 5, the vertical wind variances (Fig. 5b) in ACE-ENA winter (layer-mean of
542 $0.244 \text{ m}^2 \text{ s}^{-2}$) are generally higher than those in summer ($0.153 \text{ m}^2 \text{ s}^{-2}$) and SOCRATES ($0.147 \text{ m}^2 \text{ s}^{-2}$),
543 while the horizontal wind variances (Fig. 5c & d) are comparable between ACE-ENA winter and summer
544 but much higher than the SOCRATES, resulting in higher TKE during ACE-ENA. Note that the higher
545 w'^2 near cloud top corresponds to the stronger entrainment rate in wintertime ACE-ENA. Near the cloud
546 top, turbulence effectively enhances coalescence between the larger cloud droplets, primarily by
547 increasing the relative velocities between droplets (Magaritz-Ronen et al., 2016; Ghate and Cadeddu,
548 2019), and this is especially true for the vertical component w'^2 of TKE. While the horizontal turbulence
549 components, the u'^2 and v'^2 can also play a role in mixing the ambient air masses and contribute to the
550 broadening of DSD (Wu et al., 2017). The use of TKE provides an illustration that in-cloud turbulence
551 during ACE-ENA might be slightly stronger than that observed during SOCRATES. That being said, the
552 quantitative evaluation of the turbulent enhancement of collision-coalescence requires access to the eddy
553 dissipation rate, as typically used in model parameterizations (Grabowski and Wang, 2013; Wittle et al.,
554 2019). The smallest scales resolvable with the 1Hz measurement used in this study are on the order of
555 140 meters, thus capturing only the larger-scale end of the inertial subrange and larger turbulent motions.
556 Consequently, the ability to resolve smaller eddies and turbulent structures, crucial for understanding the

557 energy cascade within the inertial subrange, is limited by the too-coarse spatial and temporal resolutions
558 and aliasing issues (Siebert et al., 2010; Muñoz-Esparza et al., 2018; Kim et al., 2022). Therefore, to
559 fully resolve the spectrum of turbulence and quantitatively examine energy dissipation and mixing
560 processes, access to higher-frequency measurements is required to capture smaller eddies within the
561 inertial subrange (Siebert et al., 2010; Lu et al., 2011; Waclawczyk et al., 2017). Additionally, the further
562 quantification of the entrainment-mixing mechanisms also requires high-frequency eddy dissipation and
563 accurate examination of the mixing time scale (Lehmann et al., 2009; Lu et al., 2011) for individual
564 profile. Though currently beyond the scope of this study, those mechanisms will be of interest for future
565 investigations.

566 Drizzle formation and evolution in the ACE-ENA winter clouds are noticeably stronger than in
567 the other two IOPs, which could be attributed to multiple factors. First, the ambient aerosols and CCN
568 during winter are substantially fewer, featuring clean environments that promote the formation of
569 generally larger cloud droplets due to the availability of more water content per droplet. Larger cloud
570 droplets are more likely to collide and coalesce into drizzle drops, leading to relatively heavier
571 precipitation (Chen et al., 2011; Duong et al., 2011; Mann et al., 2014). Furthermore, the wintertime
572 clouds feature deeper cloud layers with mean thickness of (392.4 m) compared to the summertime clouds
573 (336.3). In a thicker cloud layer with sufficient turbulence, the residence times of large cloud droplets
574 and drizzle drops are elongated, and the chance of collision-coalescence growth can be effectively
575 increased by recirculating the drizzle drops (Brost et al., 1982; Feingold et al., 1996; Magaritz et al.,
576 2009; Ghate et al., 2021). Additionally, the prevalence of precipitation-evaporation-induced MBL cold
577 pools, which disturb the MBL thermodynamics and contribute to turbulent mixing (Zuidema et al., 2017),
578 during the wintertime might provide strong dynamical forcing to the warm-rain process (Jenson et al.,
579 2021; J. Wang et al., 2022). As a result, the ACE-ENA wintertime drizzle DSD is sufficiently broadened,
580 and the D_{mmd} is enlarged toward the cloud base. In comparison, although the SOCRATES exhibits even

581 thicker clouds (487.4 m), the drizzle processes are seemingly suppressed by the much higher ambient
582 aerosol and CCN concentrations.

583

584 **4 Aerosol-cloud-precipitation interactions (ACPIs)**

585 **4.1 Cloud microphysical responses on aerosols**

586 The impacts of different aerosol loadings on the cloud microphysical properties can be assessed
587 by the aerosol-cloud interaction (ACI) indices, which can be quantified as:

$$588 \quad ACI_N = \frac{\partial \ln(N_c)}{\partial \ln(N_{CCN,0.35\%})}, \quad (8)$$

589 and

$$590 \quad ACI_r = -\frac{\partial \ln(r_c)}{\partial \ln(N_{CCN,0.35\%})}, \quad (9)$$

591 which emphasizes the cloud microphysical responses to CCN via the relative logarithmic change of N_c
592 and r_c to the change in $N_{CCN,0.35\%}$ (Feingold et al., 2003; McComiskey et al., 2009). Physically, the ACI
593 process involves aerosols intruding into the cloud layer, activating as cloud droplets, and subsequently
594 altering cloud DSD and dispersion (Zheng et al., 2022a&b) under various water vapor availabilities.
595 Therefore, the cloud microphysical responses within the lower region of the cloud are assessed, which is
596 the first stage in which the sub-cloud CCN can directly interact with the cloud droplets. Furthermore, the
597 similarity in the vertical integral of LWC_c (as shown in Fig. 3c) provides comparable liquid water
598 between three IOPs for the assessment of newly generated cloud embryos from activated CCN because
599 the ACI_r is normally assessed under a fixed liquid water (Zheng et al., 2020).

600 Considering all the cases from three IOPs with available CCN measurements (some cases without
601 CCN measurements during SOCRATES), the N_c and r_c at the lower cloud ($z_i < 0.2$) are plotted against
602 the sub-cloud $N_{CCN,0.35\%}$ in Figure 6, and the ACI indices are calculated as $ACI_{N,CB}$ and $ACI_{r,CB}$ (CB
603 denoting the assessment near the cloud base). Note that the availability of valid sub-cloud measurements
604 inevitably limits the sample size, especially for SOCRATES, as shown in Table S2. As shown in Figure

605 6a, the $ACI_{N,CB}$ for the ACE-ENA wintertime (0.748) is higher than the summertime (0.617), indicating
606 that N_c is more sensitive to the sub-cloud $N_{CCN,0.35\%}$ during the winter. In other words, aerosols intruding
607 into the cloud layer are easily activated to become cloud droplets. The N_c sensitivity for the SOCRATES
608 cloud (0.692) lies between the two ACE-ENA IOPs. The $ACI_{N,CB}$ values from three IOPs are generally
609 higher than the ACI_N values from the layer-mean N_c against the sub-cloud $N_{CCN,0.35\%}$ (not shown).
610 Previous studies have shown that the enhanced vertical turbulence (updraft velocity) can effectively
611 facilitate CCN replenishment into the cloud layer (Hu et al., 2021; Zheng et al., 2022a&b) and increase
612 the actual in-cloud supersaturation (Brunke et al., 2022), thus leading to a more efficient cloud droplet
613 formation, enhancing the $ACI_{N,CB}$. By correlating the mean TKE values with the CCN activation ratio
614 ($N_c/N_{CCN,0.35\%}$) for all individual cloud cases, the three IOPs show moderate but statistically significant
615 correlation coefficients of 0.36, 0.55, and 0.51 for ACE-ENA summer, winter, and SOCRATES,
616 respectively. This result reinforces the notion that the CCN activation fractions, particularly during the
617 wintertime ACE-ENA, are significantly correlated with in-cloud turbulence intensities. Furthermore,
618 more coarse mode aerosols during ACE-ENA winter are also favorable to the activation efficiency
619 (Dusek et al., 2006).

620 As for the r_c responses to CCN (Fig. 6b), the typical Twomey effect, where more CCN compete
621 against available water vapor and result in smaller cloud droplets, is evidenced by different cloud
622 susceptibility between the three IOPs. The SOCRATES features a higher $ACI_{r,CB}$ (0.311), suggesting
623 that an increase in $N_{CCN,0.35\%}$ can result in a significant decrease in r_c , compared to ACE-ENA summer
624 (0.206) and winter (0.263). Although the absolute range of variation for r_c during SOCRATES is smaller,
625 the slope is much deeper (Fig. 6b). Recall that the sub-cloud $N_{CCN,0.35\%}$ during SOCRATES is generally
626 higher and is constituted by more small-sized aerosols (as indicated in Fig. 2b). Consequently, after
627 activation, the lower part of the cloud exhibits a higher number of smaller cloud droplets, as shown in
628 Fig. 4d, even under the relatively less $N_{CCN,0.35\%}$ condition for SOCRATES. Therefore, as more CCN

629 intrudes into the cloud, the competition for water vapor among newly-activated cloud droplets becomes
630 more pronounced, given similar water availability. In contrast, the presence of larger cloud droplets near
631 the cloud base, whether activated from coarse-mode aerosols or remaining as residuals from collision-
632 coalescence, would elevate the r_c especially under the relatively more CCN condition, hence inevitably
633 dampening the $ACI_{r,CB}$ during ACE-ENA. However, a more comprehensive investigation into the cloud
634 microphysical responses to CCN intrusions under a larger range of various water supply conditions, and
635 further untangling the ACI from the meteorological influences, will require additional aircraft cases from
636 more field campaigns, for instance the VAMOS Ocean-Cloud-Atmosphere-Land Study (VOCALS), the
637 Cloud System Evolution over the Trades (CSET), the ObseRvations of CLOUDs above Aerosols and their
638 intERactionS (ORACLES), and the Aerosol Cloud meTeorology Interactions oVer the western ATlantic
639 Experiment (ACTIVATE). Note that the $ACI_{r,CB}$ values in Figure 6b are also larger than the results from
640 the layer-mean r_c against sub-cloud $N_{CCN,0.35\%}$, since the layer-mean microphysics is more subject to the
641 cloud droplet evolution processes such as condensational growth and collision-coalescence. The ACI
642 indices from three IOPs are in the ACI range of the previous studies in MBL clouds (Twohy et al., 2005;
643 Lu et al., 2009; Diamond et al., 2018) using aircraft in-situ measurements.

644 To investigate the ACI indices at the upper level of the cloud, the N_c and r_c at the upper cloud
645 ($z_i > 0.8$) are plotted against the above-cloud $N_{CCN,0.35\%}$ in Figure S5, and the ACI indices are calculated
646 as $ACI_{N,CT}$ and $ACI_{r,CT}$ (denoting the assessments near the cloud top). Compared to the $ACI_{N,CB}$ and
647 $ACI_{r,CB}$, the $ACI_{N,CT}$ and $ACI_{r,CT}$ are much weaker, especially for $ACI_{r,CT}$, as the near cloud top droplets
648 are too large for above-cloud aerosols to exert a significant influence on r_c (Diamond et al., 2018; Gupta
649 et al., 2022). While the weaker cloud top N_c dependence on the $N_{CCN,0.35\%}$ could be due to the legacy of
650 the sub-cloud CCN impacts on N_c being conveyed to the cloud top. This occurs because FT aerosols and
651 CCN can be entrained down to the MBL before and during the cloud process, as observed in the
652 assessment of inter-cloud cases. These weaker relationships support the notion that though the aerosols

653 entrained into the upper-cloud region can affect the cloud microphysics to a certain degree, the effects
654 are less pronounced than those from the sub-cloud aerosols (Diamond et al., 2018, Wang et al., 2020)
655 because the MBL cloud N_c and r_c variations are dominated by the condensational growth process,
656 collision-coalescence process, and cloud top entrainment mixing near the cloud top.

657

658 **4.2 Precipitation susceptibility**

659 The precipitation susceptibility relies on the assessment of relative responses in the precipitation
660 rate to the change in N_c (Feingold and Seibert, 2009; Sorooshian et al., 2009), which is defined as:

$$661 S_o = -\frac{\partial \ln(R_{CB})}{\partial \ln(N_c)}, \quad (10)$$

662 where the R_{CB} is the cloud base precipitation rate calculated in section 2 (equation 5). By incorporating
663 all the cloud cases, including both precipitating and non-precipitating clouds (the R_{CB} can also be
664 calculated based on the drizzle DSD near the cloud base), the S_o accounts for the impact of cloud droplets
665 on the potential precipitation ability of the cloud (Terai et al., 2012).

666 As shown in Figure 7a, the R_{CB} values generally have a negative correlation with increased layer-
667 mean N_c for all three IOPs. The S_o values are 0.979, 1.229, and 1.638, with the absolute values of
668 correlation coefficients being 0.33, 0.29, and 0.45 for SOCRATES, ACE-ENA summer and winter,
669 respectively. These correlation coefficient values fall within the reasonable range found in previous
670 studies on precipitation susceptibility in MBL stratus and stratocumulus clouds (Jung et al., 2016; Gupta
671 et al., 2022), and indicate statistically significant dependences of R_{CB} on N_c . Previous study by Terai et
672 al. (2012) found that the S_o values decrease with the increasing cloud thickness over the southeast Pacific,
673 and Jung et al. (2016) found that the S_o is more pronounced within the medium-deep clouds with
674 thickness ~ 300 -400 m in the MBL stratocumulus over the eastern Pacific. While Gupta et al. (2022)
675 found that the S_o values are generally higher under low ambient N_a condition in the southeastern Atlantic
676 MBL. In this study, R_{CB} for the ACE-ENA winter is more susceptible to the layer-mean N_c than the

677 ACE-ENA summer and SOCRATES, which can be partially attributed to the existence of more large
678 drizzle drops (as shown in Fig. 4d) near the cloud base. As previously discussed, the ACE-ENA winter
679 feature with enhanced collision-coalescence and the drizzle-recirculating processes, especially under low
680 N_c conditions with more larger drizzle drops, leading to the increase of S_o values. In comparison, the
681 higher ambient aerosol and CCN concentrations during SOCRATES lead to relatively narrower drizzle
682 DSDs and may induce effective aerosol buffering effects, where the warm-rain processes in cloud are
683 already fairly suppressed, hence diminishing the sensitivity of R_{CB} to N_c (Stevens and Feingold, 2009;
684 Fan et al., 2020; Gupta et al., 2022).

685 In addition, it is well known that the R_{CB} can be parameterized or predicted via an approximate
686 relation with N_c and cloud thickness (H_c), which is usually parameterized in the form of $R_{CB} \propto c H_c^3 N_c^{-1}$
687 (Lu et al., 2009). Following the same method, we derive the relationships from three IOPs in Figure 7b,
688 where the R_{CB} are positively (negatively) proportional to the H_c (N_c), with the exponential parameters in
689 the range of the typical values in the MBL clouds (Comstock et al., 2004; vanZanten et al., 2005; Lu et
690 al., 2009). The statistical R^2 values of R_{CB} against H_c (N_c) are 0.696 (0.177), 0.419 (0.212) and 0.165
691 (0.295), for the ACE-ENA summer, winter and SOCRATES, respectively, suggesting that the R_{CB} in
692 ACE-ENA clouds may be more determined by H_c , while the R_{CB} in SOCRATES cloud are more related
693 to N_c . Note that the relationship for SOCRATES in this study reveals a similar R_{CB} dependence on N_c
694 but a smaller dependence on the cloud thickness than the study by Kang et al. (2024), who concluded a
695 relationship of $R_{CB} = 1.73e^{-10} H_c^{3.6} N_c^{-1}$, based on the rain rate retrieved from radar and lidar
696 measurements and the aerosol concentration also from the SOCRATES. The discrepancies are possibly
697 due to the different sample selections and different methods in the R_{CB} calculation. Note that the mean
698 cloud thicknesses of the ACE-ENA summer (336.3 m), winter (392.4 m) and SOCRATES (487.4 m),
699 are within the thickness range where is found to exhibit stronger S_o (Terai et al., 2012; Jung et al., 2016;
700 Gupta et al., 2022).

701

702 **4.3 Drizzle impacts on sub-cloud CCN and implication to ACI**

703 Multiple studies on the MBL clouds have concluded that the in-cloud drizzle formation and
704 evolution processes can effectively impact the sub-cloud CCN budgets via the coalescence-scavenging
705 effect (Wood, 2006; Wood et al., 2012; Diamond et al., 2018; Zheng et al., 2022b; Zhang et al., 2023).
706 Drizzle drops are formed and grow via the collision-coalescence process by collecting cloud droplets and
707 small drizzle drops, resulting in the consumption of CCN (the precursor of cloud droplet), but in the
708 meantime, the in-cloud N_c can be continuously buffered by the sub-cloud CCN replenishment. Although
709 the sub-cloud aerosols (especially in large size) would be added if the drizzle fell and evaporated outside
710 the cloud, the increment cannot compensate for the loss. Therefore, the net result of the whole process is
711 usually presented as the depletion of sub-cloud CCN residuals, and such drizzle modulation on the CCN
712 budget could be substantial in moderate-to-light drizzles or even non-precipitating clouds, depending on
713 the collision-coalescence efficiency (Feingold et al., 1996; Wood, 2006; Kang et al., 2022).

714 The CCN loss rate due to the coalescence-scavenging effect can be calculated as:

$$715 L_{CCN} = -\frac{K H_c}{H_{cp}} * N_c * R_{CB}, \quad (11)$$

716 where the constant K ($2.25 \text{ m}^2 \text{ kg}^{-1}$) denotes the drizzle collection efficiency (Wood et al., 2006; Diamond
717 et al., 2018). H_c is cloud thickness, and H_{cp} is the thickness of the coupled layer to ensure the change in
718 the cloud layer can be sufficiently conveyed throughout the layer. The calculated CCN loss rate for
719 individual cases is listed in Table S2. Considering all cloud (precipitating cloud) scenarios, the mean
720 CCN loss rates are $-7.69 \pm 13.96 \text{ cm}^{-3} \text{ h}^{-1}$ ($-10.45 \pm 15.56 \text{ cm}^{-3} \text{ h}^{-1}$), $-6.29 \pm 11.65 \text{ cm}^{-3} \text{ h}^{-1}$ ($-12.11 \pm 14.64 \text{ cm}^{-3} \text{ h}^{-1}$),
721 $-4.94 \pm 7.96 \text{ cm}^{-3} \text{ h}^{-1}$ ($-5.58 \pm 8.43 \text{ cm}^{-3} \text{ h}^{-1}$) for ACE-ENA summer, winter and SOCRATES,
722 respectively. As the results indicate, the ACE-ENA clouds experience more substantial sub-cloud CCN
723 loss than SOCRATES, especially in wintertime precipitating clouds. Recall that the assessment of
724 $ACI_{r, CB}$ relies on the relative changes of r_c and N_{CCN} , while the different L_{CCN} for individual cases can

725 result in the shrinking of the N_{CCN} variation ranges (imagine the abundant CCN are depleted by the
 726 coalescence-scavenging). In other words, the given change in r_c corresponds to a narrowed change in
 727 N_{CCN} . Mathematically speaking, the assessment of $ACI_{r, CB}$ depends on the ratio of the numerator (change
 728 in r_c) and the denominator (change in N_{CCN}). Under the circumstances of substantial cloud-processing to
 729 the aerosols, the altered sub-cloud CCN budgets are reflected as a smaller denominator, versus the less
 730 altered numerator, hence mathematically presented as an enlarged $ACI_{r, CB}$. Therefore, the coalescence-
 731 scavenging effect can not only deplete the sub-cloud CCN, but also quantitatively amplify the assessment
 732 of cloud microphysics susceptibilities (Feingold et al., 1999; Duong et al., 2011; Jung et al., 2016; Zheng
 733 et al., 2022b). In order to examine the potential impact of the aforementioned processes on the ACI
 734 assessment, a sensitivity analysis is conducted by simply retrospectively the sub-cloud $N_{CCN0.35\%}$
 735 according to their L_{CCN} . For each retrospective time step ΔT , the r_c values are held unchanged, and the
 736 retrospective $N_{CCN0.35\%}$ values for individual cloud cases are given by $N_{CCN0.35\%} - L_{CCN} * \Delta T$, and then
 737 the $ACI_{r, CB}$ can be recalculated. Note that assuming a constant r_c value over time inevitably induces
 738 uncertainty and biases, as it does not consider the microphysical processes affecting the cloud droplet
 739 mean size. However, previous numerical experiments show that the noticeable impact on the cloud mean
 740 radius through collision-coalescence necessitates a high degree of CCN depletion, and the quantified
 741 percentage changes in droplet mean sizes are several times less than the changes in CCN depletion
 742 (Feingold et al., 1996). Hence, the retrospective method, from an observational snapshot point of view,
 743 provides a direction that enables the assessment of $ACI_{r, CB}$ as if before the sub-cloud aerosols and CCN
 744 are scavenged by in-cloud coalescence-scavenging and precipitation scavenging processes.

745 As shown in Figure 8, the $ACI_{r, CB}$ values tend to decrease with the retrospective time, which
 746 indicates the retrospective CCN variation range is enlarged and counteracting the coalescence-
 747 scavenging amplification. The detailed illustration of the different $ACI_{r, CB}$ calculated from the scattered
 748 r_c and sub-cloud $N_{CCN0.35\%}$ is shown in Figure S6. Note that the $ACI_{r, CB}$ decreasing rates for the

749 precipitating clouds (Fig. 8b) are not as strong as for all clouds because the non-precipitating clouds have
750 smaller L_{CCN} largely due to weaker collision-coalescence. Hence, the time retrospected might quickly
751 exceed the actual time scale of processing of cloud droplets. In other words, the time needed to store the
752 sub-cloud CCN to the budget before cloud existence is shorter. Therefore, the retrospective of the sub-
753 cloud CCN budget will yield an alternative assessment of ACI, assuming that the drizzle processes have
754 not yet significantly impacted the sub-cloud CCN budget, especially for the assessment under the
755 precipitating clouds. However, examining the exact precipitating timing is challenging since the aircraft
756 provides a snapshot of the cloud and aerosol information. Thus, this retrospective study only provides a
757 possible direction, and the result should be interpreted with caution.

758

759 **5. Summary and Conclusions**

760 Based on the aircraft in-situ measurements during ACE-ENA and SOCRATES, the vertical
761 distributions and the evolutions of the aerosol, cloud, and drizzle properties are investigated under the
762 cloud-topped MBL environments. The aerosols and CCN from SOCRATES are the highest among the
763 three IOPs, followed by ACE-ENA summer and winter in descending order in both above- and sub-cloud
764 regimes. The differences can be attributed to the differences in aerosol size distributions between ACE-
765 ENA and SOCRATES, which are largely due to the aerosol sources in those regions. The SOCRATES
766 features the pre-industrial natural environment enriched by aerosols from marine biological productivity
767 and without the contamination of anthropogenic aerosols, while the ACE-ENA features the aerosols from
768 varied sources, including maritime and continental emissions, with distinct seasonal variations.
769 Examining the aerosol size distributions in sub-cloud versus above-cloud regimes manifests the
770 significant influence of cloud processing on aerosols. Physical processing like in-cloud Brownian capture
771 can reduce Aitken mode aerosols, while the chemical processes transform Aitken mode aerosols to larger
772 sizes, moving them toward the accumulation mode. In addition, the in-cloud coalescence processes shift
773 sub-cloud aerosol residuals to larger sizes, as multiple aerosols combine into a single aerosol core inside

774 the cloud droplet during collision-coalescence, explaining the observed increase in the tail-end of the
775 aerosol distribution for all IOPs.

776 As for the cloud and drizzle properties, the SOCRATES clouds feature more and smaller cloud
777 droplets than the ACE-ENA summertime and wintertime clouds, with the r_c growths (and percentage
778 increases), from cloud base to top, being $4.03 \mu\text{m}$ (0.66%), $4.78 \mu\text{m}$ (0.68%), and $5.85 \mu\text{m}$ (0.79%) for
779 SOCRATES, ACE-ENA summer, and winter, respectively. The cloud-top entrainment mixing is
780 evidenced in the observed decline of both N_c and LWC_c near the cloud top. The mean cloud-top
781 entrainment rates (w_e) are $0.570 \pm 0.834 \text{ cm s}^{-1}$, $0.581 \pm 0.560 \text{ cm s}^{-1}$, and $0.960 \pm 1.127 \text{ cm s}^{-1}$ for
782 SOCRATES, ACE-ENA summer and winter, respectively. The strongest w_e during ACE-ENA winter is
783 owing to weaker cloud-top inversions and stronger near-cloud-top turbulence. The values of the TKE for
784 three IOPs are generally within the ranges of previous studies (Atlas et al., 2020; Ghate et al., 2021). For
785 drizzle vertical distribution, N_d from the three IOPs all exhibit decreases from cloud top to cloud base,
786 while D_{mmd} are in opposite directions with a maximum at the cloud base. The ACE-ENA wintertime
787 clouds feature more prominent drizzle formation and evolution owing to the combined effects of
788 relatively cleaner environment, deeper cloud layer, and slightly stronger in-cloud vertical turbulence,
789 which substantially enhances the collision-coalescence and the drizzle re-circulating processes,
790 compared to the other two IOPs. While satellite retrievals of droplet number concentration heavily rely
791 on the adiabatic cloud assumption and are usually given as a constant of $f_{ad} = 0.8$, the in-situ
792 observational evidence found in this study further confirms the unrealistic nature of this assumption. It
793 will be of interest to utilize multiple aircraft measurements (campaigns) to explore the variability of MBL
794 cloud and drizzle microphysical properties over different marine regions. This can help examine potential
795 predictors for f_{ad} , which will aid in satellite-based retrievals and aerosol-cloud interaction assessments
796 (Painemal and Zuidema, 2011; Grosvenor et al., 2018; Painemal et al., 2021).

797 Comparing the seasonality of cloud base precipitation rate (R_{CB}) during ACE-ENA, more cases
798 with large observed R_{CB} during the winter season, which is consistent with J. Wang et al. (2022). Notably,
799 the sensitivity of R_{CB} to N_c is more pronounced for the ACE-ENA during both winter (with $S_o = 1.638$)
800 and summer (1.229) compared to the SOCRATES ($S_o = 0.979$). This is partly due to the much higher
801 R_{CB} induced by larger drizzle drops near the cloud base for ACE-ENA, a result of turbulence-driven in-
802 cloud droplet interactions, especially under low N_c condition. Furthermore, R_{CB} can be approximated by
803 a relationship involving N_c and H_c , as suggested in prior research. The relationships established in this
804 study indicate that ACE-ENA clouds, are largely determined by H_c , while SOCRATES clouds are more
805 influenced by the N_c . The combination of a deeper cloud layer along with relatively lower ambient
806 aerosol concentration, which eventually lead to stronger drizzle production and evolution, during ACE-
807 ENA, especially during the winter season, results in more robust precipitation susceptibility. Note that
808 considering the combined factors of aerosol loadings, cloud morphology and thicknesses, and the
809 assessment methodology, the derived S_o values in this study are generally higher (or close to the upper
810 end) compared to previous studies (Lu et al., 2009; Duong et al., 2011; Terai et al., 2012; Jung et al.,
811 2016; Gupta et al., 2022).

812 The investigations of the ACI via the $ACI_{N, CB}$ and $ACI_{r, CB}$ indices reveal that during the ACE-
813 ENA wintertime, N_c is more sensitive to changes in $N_{CCN0.35\%}$, indicating aerosols more readily activate
814 to become cloud droplets compared to those in the summer, which is consistent with the previous
815 assessment by J. Wang et al. (2022) on the seasonal dependency of the relationship between N_c and
816 aerosols. One influencing factor is the strong dynamic mechanism that speeds up the infusion of CCN
817 into the cloud layer, thus aiding droplet formation. The moderate but statistically significant correlation
818 coefficients between the CCN activation fractions and the TKE agree with a previous study that found
819 the local activation fraction of CCN to be strongly associated with increased updrafts (Hu et al., 2021).
820 Furthermore, the presence of larger aerosols during ACE-ENA winter enhances the droplet activation

821 process. The SOCRATES IOP highlights a higher $ACI_{r, CB}$, indicating a pronounced decrease in r_c with
822 increasing $N_{CCN0.35\%}$. The $ACI_{r, CB}$ in ACE-ENA is dampened by the presence of more larger cloud
823 droplets near the cloud base, particularly under relatively higher $N_{CCN0.35\%}$. However, the combined
824 effect of the relatively cleaner environment and sufficient water vapor results in stronger cloud
825 microphysical responses during the ACE-ENA wintertime than in the summertime. Note that the ACI
826 indices from this study lie in the higher end of the ACI ranges estimated via remote sensing (McComiskey
827 et al., 2009; Dong et al., 2015; Zheng et al., 2022a) because the aircraft assessment of ACI is based on
828 measurements where the aerosols are in direct contact with the cloud layer. Arguably, the assessment of
829 N_c responses to $N_{CCN0.35\%}$ would inevitably be affected by the collision-coalescence process near the
830 cloud base, where simultaneously, the CCN replenishment buffers the N_c and the collision-coalescence
831 process depletes N_c . Hence, finding a layer where these two effects maintain a dynamic balance in N_c
832 might aid in a more accurate assessment and more fundamental understanding of the ACI, which might
833 be revealed by the LES or parcel model simulations.

834 Additionally, the in-cloud drizzle formation and evolution processes significantly influence the
835 sub-cloud CCN budgets via the coalescence-scavenging effect, which can potentially exaggerate the
836 assessment of cloud microphysics susceptibilities. Based on the CCN loss rate (L_{CCN}) from ACE-ENA
837 and SOCRATES, a sensitivity analysis is performed focusing on retrospectively adjusting the sub-cloud
838 CCN according to their L_{CCN} . Results showed that this adjustment led to a decreased $ACI_{r, CB}$,
839 highlighting the significance of the coalescence-scavenging process on the ACI assessment. However,
840 due to the fact that aircraft only provide a snapshot of the clouds and aerosol information, determining
841 the precise drizzle timing for the individual cloud is challenging. Hence, findings from this retrospective
842 approach provide only a direction or theory, and should be taken cautiously. Nevertheless, pursuing
843 further modeling experiments on this matter may be worthwhile. For example, the exact drizzling time
844 could be pinpointed within a model using an Eulerian framework or traced using a Lagrangian framework.

845 Nevertheless, the CCN adjustment could more accurately reflect the true characteristics of the cloud and
846 the MBL CCN budget, potentially aiding in a more precise assessment of ACI. Therefore, future works
847 would focus on the model simulation on the MBL clouds from ACE-ENA and SOCRATES and further
848 assess the modeled ACI under the observational constraints, as well as the continuous development of
849 the warm rain microphysical parameterizations, in order to aid in the better represent the MBL clouds in
850 multiple regions.

851

852

853 *Data availability.* The ACE-ENA field campaign data can be accessed from the Department of Energy
854 Atmospheric Radiation Measurement data archive ([https://iop.archive.arm.gov/arm-iop-](https://iop.archive.arm.gov/arm-iop-file/2017/ena/aceena/)
855 [file/2017/ena/aceena/](https://iop.archive.arm.gov/arm-iop-file/2017/ena/aceena/)). The SOCRATES field campaign data are publicly archived on the National
856 Center for Atmospheric Research (NCAR) Earth Observing Laboratory
857 (https://data.eol.ucar.edu/master_lists/generated/socrates/).

858

859 *Author contributions.* The original idea of this study is discussed by XZ, XD, and BX. XZ performed the
860 analyses and wrote the manuscript. XZ, XD, BX, TL, and YW participated in further scientific
861 discussions and provided substantial comments and edits on the paper.

862

863 *Competing interests.* At least one of the (co-)authors is a member of the editorial board of Atmospheric
864 Chemistry and Physics.

865

866 *Acknowledgments.* This work was supported by the NSF grants AGS-2031750/2031751/20211752 at the
867 University of Arizona, Texas A&M University and Stanford University, respectively. The authors
868 sincerely thank the investigators and mentors from the ACE-ENA and SOCRATES field campaigns for
869 making the data publicly available.

870 **References.**

- 871 Albrecht B. A.: Aerosols, Cloud Microphysics, and Fractional Cloudiness, *Science*, 245, 1227-1230,
872 10.1126/science.245.4923.1227, 1989
- 873 Albrecht, B. A., Bretherton, C. S., Johnson, D., Scubert, W. H., and Frisch, A. S.: The Atlantic
874 Stratocumulus Transition Experiment—ASTEX, *B. Am. Meteorol. Soc.*, 76, 889-904,
875 10.1175/1520-0477(1995)076<0889:Taste>2.0.Co;2, 1995.
- 876 Albrecht, B., Fang, M., and Ghate, V.: Exploring Stratocumulus Cloud-Top Entrainment Processes and
877 Parameterizations by Using Doppler Cloud Radar Observations, *J. Atmos. Sci.*, 73, 729-742,
878 10.1175/JAS-D-15-0147.1, 2016.
- 879 Atlas, R. L., Bretherton, C. S., Blossey, P. N., Gettelman, A., Bardeen, C., Lin, P., and Ming, Y.: How
880 Well Do Large-Eddy Simulations and Global Climate Models Represent Observed Boundary Layer
881 Structures and Low Clouds Over the Summertime Southern Ocean?, *Journal of Advances in*
882 *Modeling Earth Systems*, 12, e2020MS002205, <https://doi.org/10.1029/2020MS002205>, 2020.
- 883 Atlas, R., Mohrmann, J., Finlon, J., Lu, J., Hsiao, I., Wood, R., and Diao, M.: The University of
884 Washington Ice–Liquid Discriminator (UWILD) improves single-particle phase classifications of
885 hydrometeors within Southern Ocean clouds using machine learning, *Atmos. Meas. Tech.*, 14,
886 7079-7101, 10.5194/amt-14-7079-2021, 2021.
- 887 Baumgardner, D. and Korolev, A.: Airspeed Corrections for Optical Array Probe Sample Volumes, *J.*
888 *Atmos. Ocean. Tech.*, 14, 1224-1229, [https://doi.org/10.1175/1520-](https://doi.org/10.1175/1520-0426(1997)014<1224:ACFOAP>2.0.CO;2)
889 [0426\(1997\)014<1224:ACFOAP>2.0.CO;2](https://doi.org/10.1175/1520-0426(1997)014<1224:ACFOAP>2.0.CO;2), 1997.
- 890 Baumgardner, D., Abel, S. J., Axisa, D., Cotton, R., Crosier, J., Field, P., Gurganus, C., Heymsfield, A.,
891 Korolev, A., Krämer, M., Lawson, P., McFarquhar, G., Ulanowski, Z., and Um, J.: Cloud Ice
892 Properties: In Situ Measurement Challenges, *Meteor. Monogr.*, 58, 9.1-9.23,
893 <https://doi.org/10.1175/AMSMONOGRAPHS-D-16-0011.1>, 2017.

894 Braun, R. A., Dadashazar, H., MacDonald, A. B., Crosbie, E., Jonsson, H. H., Woods, R. K., Flagan, R.
895 C., Seinfeld, J. H., and Sorooshian, A.: Cloud Adiabaticity and Its Relationship to Marine
896 Stratocumulus Characteristics Over the Northeast Pacific Ocean, *J. Geophys. Res.-Atmos.*, 123,
897 13790 - 13806, 10.1029/2018jd029287, 2018.

898 Brenguier, J. L., Burnet, F., and Geoffroy, O.: Cloud optical thickness and liquid water path – does the k
899 coefficient vary with droplet concentration?, *Atmos. Chem. Phys.*, 11, 9771-9786, 10.5194/acp-11-
900 9771-2011, 2011.

901 Brost, R. A., Wyngaard, J. C., and Lenschow, D. H.: Marine Stratocumulus Layers. Part II: Turbulence
902 Budgets, *J. Atmos. Sci.*, 39, 818-836, 10.1175/1520-0469(1982)039<0818:MSLPIT>2.0.CO;2,
903 1982.

904 Brunke, M. A., Cutler, L., Urzua, R. D., Corral, A. F., Crosbie, E., Hair, J., Hostetler, C., Kirschler, S.,
905 Larson, V., Li, X.-Y., Ma, P.-L., Minke, A., Moore, R., Robinson, C. E., Scarino, A. J., Schlosser,
906 J., Shook, M., Sorooshian, A., Lee Thornhill, K., Voigt, C., Wan, H., Wang, H., Winstead, E., Zeng,
907 X., Zhang, S., and Ziemba, L. D.: Aircraft Observations of Turbulence in Cloudy and Cloud-Free
908 Boundary Layers Over the Western North Atlantic Ocean From ACTIVATE and Implications for
909 the Earth System Model Evaluation and Development, *J. Geophys. Res.-Atmos.*, 127,
910 e2022JD036480, <https://doi.org/10.1029/2022JD036480>, 2022.

911 Chen, J., Liu, Y., Zhang, M., and Peng, Y.: Height Dependency of Aerosol-Cloud Interaction Regimes,
912 *J. Geophys. Res.-Atmos.*, 123, 491-506, <https://doi.org/10.1002/2017JD027431>, 2018.

913 Chen, S., Yau, M. K., and Bartello, P.: Turbulence Effects of Collision Efficiency and Broadening of
914 Droplet Size Distribution in Cumulus Clouds, *J. Atmos. Sci.*, 75, 203-217,
915 <https://doi.org/10.1175/JAS-D-17-0123.1>, 2018.

916 Chen, Y. C., Xue, L., Lebo, Z. J., Wang, H., Rasmussen, R. M., and Seinfeld, J. H.: A comprehensive
917 numerical study of aerosol-cloud-precipitation interactions in marine stratocumulus, *Atmos. Chem.*
918 *Phys.*, 11, 9749-9769, 10.5194/acp-11-9749-2011, 2011.

919 Christensen, M. W., Ma, P. L., Wu, P., Varble, A. C., Mülmenstädt, J., and Fast, J. D.: Evaluation of
920 aerosol–cloud interactions in E3SM using a Lagrangian framework, *Atmos. Chem. Phys.*, 23, 2789-
921 2812, 10.5194/acp-23-2789-2023, 2023.

922 Comstock, K. K., Wood, R., Yuter, S. E., and Bretherton, C. S.: Reflectivity and rain rate in and below
923 drizzling stratocumulus, *Q. J. R. Meteor. Soc.*, 130, 2891-2918, <https://doi.org/10.1256/qj.03.187>,
924 2004.

925 Cooper, W. A., Friesen, R. B., Hayman, M., Jensen, J., Lenschow, D. H., Romashkin, P., Schanot, A., Spuler, S.,
926 Stith, J., and Wolff, C.: Characterization of Uncertainty in Measurements of Wind from the NSF/NCAR
927 Gulfstream V Research Aircraft (No. NCAR/TN-528+STR), NCAR Technical Notes,
928 doi:10.5065/D60G3HJ8, 2016.

929 Covert, D. S., Kapustin, V. N., Bates, T. S., and Quinn, P. K.: Physical properties of marine boundary
930 layer aerosol particles of the mid-Pacific in relation to sources and meteorological transport, *J.*
931 *Geophys. Res.-Atmos.*, 101, 6919-6930, <https://doi.org/10.1029/95JD03068>, 1996.

932 D'Alessandro, J. J., McFarquhar, G. M., Wu, W., Stith, J. L., Jensen, J. B., and Rauber, R. M.:
933 Characterizing the Occurrence and Spatial Heterogeneity of Liquid, Ice, and Mixed Phase Low-
934 Level Clouds Over the Southern Ocean Using in Situ Observations Acquired During SOCRATES,
935 *J. Geophys. Res.-Atmos.*, 126, e2020JD034482, <https://doi.org/10.1029/2020JD034482>, 2021.

936 Danker, J., Sourdeval, O., McCoy, I. L., Wood, R., and Possner, A.: Exploring relations between cloud
937 morphology, cloud phase, and cloud radiative properties in Southern Ocean's stratocumulus clouds,
938 *Atmos. Chem. Phys.*, 22, 10247-10265, 10.5194/acp-22-10247-2022, 2022.

939 Desai, N., Liu, Y., Glienke, S., Shaw, R. A., Lu, C., Wang, J., and Gao, S.: Vertical Variation of Turbulent
940 Entrainment Mixing Processes in Marine Stratocumulus Clouds Using High-Resolution Digital
941 Holography, *J. Geophys. Res.-Atmos.*, 126, e2020JD033527,
942 <https://doi.org/10.1029/2020JD033527>, 2021.

943 Dong, X., Schwantes, A. C., Xi, B., and Wu, P.: Investigation of the marine boundary layer cloud and
944 CCN properties under coupled and decoupled conditions over the Azores, *J. Geophys. Res.-Atmos.*,
945 120, 6179-6191, <https://doi.org/10.1002/2014JD022939>, 2015.

946 Dong, X., X. Zheng, B. Xi, and S. Xie (2023), A Climatology of Midlatitude Maritime Cloud Fraction and
947 Radiative Effect Derived from the ARM ENA Ground-Based Observations, *J. Climate*, 36(2), 531-546,
948 doi:10.1175/JCLI-D-22-0290.1.

949 Duong, H. T., Sorooshian, A., and Feingold, G.: Investigating potential biases in observed and modeled
950 metrics of aerosol-cloud-precipitation interactions, *Atmos. Chem. Phys.*, 11, 4027-4037,
951 10.5194/acp-11-4027-2011, 2011.

952 Fan, C., Wang, M., Rosenfeld, D., Zhu, Y., Liu, J., and Chen, B.: Strong Precipitation Suppression by
953 Aerosols in Marine Low Clouds, *Geophys. Res. Lett.*, 47, e2019GL086207,
954 <https://doi.org/10.1029/2019GL086207>, 2020.

955 Feingold, G., Frisch, A. S., Stevens, B., and Cotton, W. R.: On the relationship among cloud turbulence,
956 droplet formation and drizzle as viewed by Doppler radar, microwave radiometer and lidar, *J.*
957 *Geophys. Res.-Atmos.*, 104, 22195-22203, <https://doi.org/10.1029/1999JD900482>, 1999.

958 Feingold, G., Kreidenweis, S. M., Stevens, B., and Cotton, W. R.: Numerical simulations of
959 stratocumulus processing of cloud condensation nuclei through collision-coalescence, *J. Geophys.*
960 *Res.-Atmos.*, 101, 21391-21402, <https://doi.org/10.1029/96JD01552>, 1996.

961 Feingold, G. and McComiskey, A.: ARM's Aerosol-Cloud-Precipitation Research (Aerosol Indirect Effects),
962 *Meteor. Monogr.*, 57, 22.21-22.15, 10.1175/AMSMONOGRAPHS-D-15-0022.1, 2016.

963 Feingold, G. and Siebert, H.: Cloud – Aerosol Interactions from the Micro to the Cloud Scale, from the
964 Strungmann Forum Report, *Clouds in the Perturbed Climate System: Their Relationship to Energy*
965 *Balance, Atmospheric Dynamics, and Precipitation*, 2, edited by: Heintzenberg, J. and Charlson, R.
966 J., MIT Press, ISBN 978-0-262-01287-4, 2009.

967 Flossmann, A. I., Hall, W. D., and Pruppacher, H. R.: A Theoretical Study of the Wet Removal of
968 Atmospheric Pollutants. Part I: The Redistribution of Aerosol Particles Captured through
969 Nucleation and Impaction Scavenging by Growing Cloud Drops, *J. Atmos. Sci.*, 42, 583-606,
970 [https://doi.org/10.1175/1520-0469\(1985\)042<0583:ATSOTW>2.0.CO;2](https://doi.org/10.1175/1520-0469(1985)042<0583:ATSOTW>2.0.CO;2), 1985.

971 Gao, S., Lu, C., Liu, Y., Mei, F., Wang, J., Zhu, L., and Yan, S.: Contrasting Scale Dependence of
972 Entrainment-Mixing Mechanisms in Stratocumulus Clouds, *Geophys. Res. Lett.*, 47,
973 e2020GL086970, <https://doi.org/10.1029/2020GL086970>, 2020.

974 Ghate, V. P. and Cadetdu, M. P.: Drizzle and Turbulence Below Closed Cellular Marine Stratocumulus
975 Clouds, *J. Geophys. Res.-Atmos.*, 124, 5724-5737, <https://doi.org/10.1029/2018JD030141>, 2019.

976 Ghate, V. P., Cadetdu, M. P., Zheng, X., and O'Connor, E.: Turbulence in the Marine Boundary Layer
977 and Air Motions below Stratocumulus Clouds at the ARM Eastern North Atlantic Site, *J. Appl.*
978 *Meteorol. Clim.*, 60, 1495-1510, 10.1175/JAMC-D-21-0087.1, 2021.

979 Grabowski, W. W. and Wang, L.-P.: Growth of Cloud Droplets in a Turbulent Environment, *Annual*
980 *Review of Fluid Mechanics*, 45, 293-324, 10.1146/annurev-fluid-011212-140750, 2013.

981 Grosvenor, D. P., Sourdeval, O., Zuidema, P., Ackerman, A., Alexandrov, M. D., Bennartz, R., Boers,
982 R., Cairns, B., Chiu, J. C., Christensen, M., Deneke, H., Diamond, M., Feingold, G., Fridlind, A.,
983 H unerbein, A., Knist, C., Kollias, P., Marshak, A., McCoy, D., Merk, D., Painemal, D., Rausch, J.,
984 Rosenfeld, D., Russchenberg, H., Seifert, P., Sinclair, K., Stier, P., van Diedenhoven, B., Wendisch,
985 M., Werner, F., Wood, R., Zhang, Z., and Quaas, J.: Remote Sensing of Droplet Number
986 Concentration in Warm Clouds: A Review of the Current State of Knowledge and Perspectives,
987 *Reviews of Geophysics*, 56, 409-453, <https://doi.org/10.1029/2017RG000593>, 2018.

988 Gupta, S., McFarquhar, G. M., O'Brien, J. R., Delene, D. J., Poellot, M. R., Dobracki, A., Podolske, J.
989 R., Redemann, J., LeBlanc, S. E., Segal-Rozenhaimer, M., and Pistone, K.: Impact of the variability
990 in vertical separation between biomass burning aerosols and marine stratocumulus on cloud

991 microphysical properties over the Southeast Atlantic, *Atmos. Chem. Phys.*, 21, 4615– 4635,
992 <https://doi.org/10.5194/acp-21-4615-2021>, 2021.

993 Gupta, S., McFarquhar, G. M., O'Brien, J. R., Poellot, M. R., Delene, D. J., Miller, R. M., and Small
994 Griswold, J. D.: Factors affecting precipitation formation and precipitation susceptibility of marine
995 stratocumulus with variable above- and below-cloud aerosol concentrations over the Southeast
996 Atlantic, *Atmos. Chem. Phys.*, 22, 2769–2793, <https://doi.org/10.5194/acp-22-2769-2022>, 2022.

997 Hansen, J. E. and Travis, L. D.: Light scattering in planetary atmospheres, *Space Sci. Rev.*, 16, 527-610,
998 [doi:10.1007/BF00168069](https://doi.org/10.1007/BF00168069), 1974.

999 Hill, A. A., Feingold, G., and Jiang, H.: The Influence of Entrainment and Mixing Assumption on
1000 Aerosol–Cloud Interactions in Marine Stratocumulus, *J. Atmos. Sci.*, 66, 1450-1464,
1001 [10.1175/2008JAS2909.1](https://doi.org/10.1175/2008JAS2909.1), 2009.

1002 Hinds, W.C.: *Aerosol Technology, Properties, Behaviour, and Measurement of Airborne Particles*. John
1003 Wiley & Sons Inc., New York., 1999.

1004 Hoffmann, F. and Feingold, G.: A Note on Aerosol Processing by Droplet Collision-Coalescence,
1005 *Geophys. Res. Lett.*, 50, e2023GL103716, <https://doi.org/10.1029/2023GL103716>, 2023.

1006 Hu, A. Z., Igel, A. L., Chuang, P. Y., and Witte, M. K.: Recognition of Inter-Cloud Versus Intra-Cloud
1007 Controls on Droplet Dispersion With Applications to Microphysics Parameterization, *J. Geophys.*
1008 *Res.-Atmos.*, 126, e2021JD035180, <https://doi.org/10.1029/2021JD035180>, 2021.

1009 Hudson, J. G. and Noble, S.: CCN Spectral Shape and Cumulus Cloud and Drizzle Microphysics, *J.*
1010 *Geophys. Res.-Atmos.*, 125, e2019JD031141, <https://doi.org/10.1029/2019JD031141>, 2020.

1011 Jensen, M. P., Ghate, V. P., Wang, D., Apoznanski, D. K., Bartholomew, M. J., Giangrande, S. E.,
1012 Johnson, K. L., and Thieman, M. M.: Contrasting characteristics of open- and closed-cellular
1013 stratocumulus cloud in the eastern North Atlantic, *Atmos. Chem. Phys.*, 21, 14557-14571,
1014 [10.5194/acp-21-14557-2021](https://doi.org/10.5194/acp-21-14557-2021), 2021.

1015 Jones, C. R., Bretherton, C. S., and Leon, D.: Coupled vs. decoupled boundary layers in VOCALS-REx,
1016 Atmos. Chem. Phys., 11, 7143-7153, 10.5194/acp-11-7143-2011, 2011.

1017 Jung, E., Albrecht, B. A., Sorooshian, A., Zuidema, P., and Jonsson, H. H.: Precipitation susceptibility
1018 in marine stratocumulus and shallow cumulus from airborne measurements, Atmos. Chem. Phys.,
1019 16, 11395-11413, 10.5194/acp-16-11395-2016, 2016.

1020 Kang, L., Marchand, R. T., Wood, R., and McCoy, I. L.: Coalescence Scavenging Drives Droplet
1021 Number Concentration in Southern Ocean Low Clouds, Geophys. Res. Lett., 49, e2022GL097819,
1022 <https://doi.org/10.1029/2022GL097819>, 2022.

1023 Kang, L., Marchand, R. T., and Wood, R.: Stratocumulus Precipitation Properties Over the Southern
1024 Ocean Observed From Aircraft During the SOCRATES Campaign, J. Geophys. Res.-Atmos., 129,
1025 e2023JD039831, <https://doi.org/10.1029/2023JD039831>, 2024.

1026 Kim, S. H., Kim, J., Kim, J. H., and Chun, H. Y.: Characteristics of the derived energy dissipation rate
1027 using the 1 Hz commercial aircraft quick access recorder (QAR) data, Atmos. Meas. Tech.,
1028 15, 2277-2298, 10.5194/amt-15-2277-2022, 2022.

1029 Lang, F., Ackermann, L., Huang, Y., Truong, S. C. H., Siems, S. T., and Manton, M. J.: A climatology
1030 of open and closed mesoscale cellular convection over the Southern Ocean derived from Himawari-
1031 8 observations, Atmos. Chem. Phys., 22, 2135-2152, 10.5194/acp-22-2135-2022, 2022.

1032 Lu, C., Zhu, L., Liu, Y., Mei, F., Fast, J. D., Pekour, M. S., Luo, S., Xu, X., He, X., Li, J., and Gao, S.:
1033 Observational study of relationships between entrainment rate, homogeneity of mixing, and cloud
1034 droplet relative dispersion, Atmos. Res., 293, 106900,
1035 <https://doi.org/10.1016/j.atmosres.2023.106900>, 2023.

1036 Lu, M.-L., Sorooshian, A., Jonsson, H. H., Feingold, G., Flagan, R. C., and Seinfeld, J. H.: Marine
1037 stratocumulus aerosol-cloud relationships in the MASE-II experiment: Precipitation susceptibility
1038 in eastern Pacific marine stratocumulus, J. Geophys. Res.-Atmos., 114,
1039 <https://doi.org/10.1029/2009JD012774>, 2009.

1040 Mann, J. A. L., Christine Chiu, J., Hogan, R. J., O'Connor, E. J., L'Ecuyer, T. S., Stein, T. H. M., and
1041 Jefferson, A.: Aerosol impacts on drizzle properties in warm clouds from ARM Mobile Facility
1042 maritime and continental deployments, *J. Geophys. Res.-Atmos.*, 119, 4136-4148,
1043 <https://doi.org/10.1002/2013JD021339>, 2014.

1044 Mechem, D. B., Wittman, C. S., Miller, M. A., Yuter, S. E., and de Szoeke, S. P.: Joint Synoptic and
1045 Cloud Variability over the Northeast Atlantic near the Azores, *J. Appl. Meteorol. Clim.*, 57, 1273-
1046 1290, <https://doi.org/10.1175/JAMC-D-17-0211.1>, 2018.

1047 McComiskey, A., Feingold, G., Frisch, A. S., Turner, D. D., Miller, M. A., Chiu, J. C., Min, Q., and
1048 Ogren, J. A.: An assessment of aerosol-cloud interactions in marine stratus clouds based on surface
1049 remote sensing, *J. Geophys. Res.-Atmos.*, 114, <https://doi.org/10.1029/2008JD011006>, 2009.

1050 McCoy, I. L., Wood, R., and Fletcher, J. K.: Identifying Meteorological Controls on Open and Closed
1051 Mesoscale Cellular Convection Associated with Marine Cold Air Outbreaks, *J. Geophys. Res.-*
1052 *Atmos.*, 122, 11,678-611,702, <https://doi.org/10.1002/2017JD027031>, 2017.

1053 McCoy, I. L., McCoy, D. T., Wood, R., Regayre, L., Watson-Parris, D., Grosvenor, D. P., Mulcahy, J.
1054 P., Hu, Y., Bender, F. A. M., Field, P. R., Carslaw, K. S., and Gordon, H.: The hemispheric contrast
1055 in cloud microphysical properties constrains aerosol forcing, *P. Natl. Acad. Sci. USA*, 117, 18998-
1056 19006, [10.1073/pnas.1922502117](https://doi.org/10.1073/pnas.1922502117), 2020.

1057 McCoy, I. L., Bretherton, C. S., Wood, R., Twohy, C. H., Gettelman, A., Bardeen, C. G., and Toohey,
1058 D. W.: Influences of Recent Particle Formation on Southern Ocean Aerosol Variability and Low
1059 Cloud Properties, *J. Geophys. Res.-Atmos.*, 126, e2020JD033529,
1060 <https://doi.org/10.1029/2020JD033529>, 2021.

1061 McFarquhar, G. M., Bretherton, C. S., Marchand, R., Protat, A., DeMott, P. J., Alexander, S. P., Roberts,
1062 G. C., Twohy, C. H., Toohey, D., Siems, S., Huang, Y., Wood, R., Rauber, R. M., Lasher-Trapp,
1063 S., Jensen, J., Stith, J. L., Mace, J., Um, J., Järvinen, E., Schnaiter, M., Gettelman, A., Sanchez, K.
1064 J., McCluskey, C. S., Russell, L. M., McCoy, I. L., Atlas, R. L., Bardeen, C. G., Moore, K. A., Hill,

1065 T. C. J., Humphries, R. S., Keywood, M. D., Ristovski, Z., Cravigan, L., Schofield, R., Fairall, C.,
1066 Mallet, M. D., Kreidenweis, S. M., Rainwater, B., D'Alessandro, J., Wang, Y., Wu, W., Saliba, G.,
1067 Levin, E. J. T., Ding, S., Lang, F., Truong, S. C. H., Wolff, C., Haggerty, J., Harvey, M. J.,
1068 Klekociuk, A. R., and McDonald, A.: Observations of Clouds, Aerosols, Precipitation, and Surface
1069 Radiation over the Southern Ocean: An Overview of CAPRICORN, MARCUS, MICRE, and
1070 SOCRATES, *B. Am. Meteorol. Soc.*, 102, E894-E928, [https://doi.org/10.1175/BAMS-D-20-](https://doi.org/10.1175/BAMS-D-20-0132.1)
1071 0132.1, 2021.

1072 Muñoz-Esparza, D., Sharman, R. D., and Lundquist, J. K.: Turbulence Dissipation Rate in the
1073 Atmospheric Boundary Layer: Observations and WRF Mesoscale Modeling during the XPIA Field
1074 Campaign, *Mon. Weather Rev.*, 146, 351-371, <https://doi.org/10.1175/MWR-D-17-0186.1>, 2018.

1075 Olfert, J. S., Kulkarni, P., and Wang, J.: Measuring aerosol size distributions with the fast integrated
1076 mobility spectrometer, *Journal of Aerosol Science*, 39, 940-956,
1077 <https://doi.org/10.1016/j.jaerosci.2008.06.005>, 2008.

1078 Painemal, D. and Zuidema, P.: Assessment of MODIS cloud effective radius and optical thickness
1079 retrievals over the Southeast Pacific with VOCALS-REx in situ measurements, *J. Geophys. Res.-*
1080 *Atmos.*, 116, <https://doi.org/10.1029/2011JD016155>, 2011.

1081 Painemal, D., Chang, F. L., Ferrare, R., Burton, S., Li, Z., Smith Jr, W. L., Minnis, P., Feng, Y., and
1082 Clayton, M.: Reducing uncertainties in satellite estimates of aerosol–cloud interactions over the
1083 subtropical ocean by integrating vertically resolved aerosol observations, *Atmos. Chem. Phys.*, 20,
1084 7167-7177, [10.5194/acp-20-7167-2020](https://doi.org/10.5194/acp-20-7167-2020), 2020.

1085 Painemal, D., Spangenberg, D., Smith Jr, W. L., Minnis, P., Cairns, B., Moore, R. H., Crosbie, E.,
1086 Robinson, C., Thornhill, K. L., Winstead, E. L., and Ziemba, L.: Evaluation of satellite retrievals of
1087 liquid clouds from the GOES-13 imager and MODIS over the midlatitude North Atlantic during the
1088 NAAMES campaign, *Atmos. Meas. Tech.*, 14, 6633-6646, [10.5194/amt-14-6633-2021](https://doi.org/10.5194/amt-14-6633-2021), 2021.

1089 Pinsky, M. B. and Khain, A. P.: Turbulence effects on droplet growth and size distribution in clouds—
1090 A review, *Journal of Aerosol Science*, 28, 1177-1214, <https://doi.org/10.1016/S0021->
1091 8502(97)00005-0, 1997.

1092 Pruppacher, H. R. and Klett, J. D.: *Microphysics of clouds and precipitation*, Kluwer Academic
1093 Publishers, Dordrecht, the Netherlands, 1997.

1094 Rémillard, J. and Tselioudis, G.: Cloud Regime Variability over the Azores and Its Application to
1095 Climate Model Evaluation, *J. Climate*, 28, 9707-9720, <https://doi.org/10.1175/JCLI-D-15-0066.1>,
1096 2015.

1097 Sanchez, K. J., Roberts, G. C., Diao, M., and Russell, L. M.: Measured Constraints on Cloud Top
1098 Entrainment to Reduce Uncertainty of Nonprecipitating Stratocumulus Shortwave Radiative
1099 Forcing in the Southern Ocean, *Geophys. Res. Lett.*, 47, e2020GL090513,
1100 <https://doi.org/10.1029/2020GL090513>, 2020.

1101 Sanchez, K. J., Roberts, G. C., Saliba, G., Russell, L. M., Twohy, C., Reeves, J. M., Humphries, R. S.,
1102 Keywood, M. D., Ward, J. P., and McRobert, I. M.: Measurement report: Cloud processes and the
1103 transport of biological emissions affect southern ocean particle and cloud condensation nuclei
1104 concentrations, *Atmos. Chem. Phys.*, 21, 3427-3446, 10.5194/acp-21-3427-2021, 2021.

1105 Stevens, B. and Feingold, G.: Untangling aerosol effects on clouds and precipitation in a buffered system,
1106 *Nature*, 461, 607-613, 10.1038/nature08281, 2009.

1107 Siebert, H., Shaw, R. A., and Warhaft, Z.: Statistics of Small-Scale Velocity Fluctuations and Internal
1108 Intermittency in Marine Stratocumulus Clouds, *J. Atmos. Sci.*, 67, 262-273,
1109 <https://doi.org/10.1175/2009JAS3200.1>, 2010.

1110 Sorooshian, A., Feingold, G., Lebsock, M. D., Jiang, H., and Stephens, G. L.: On the precipitation
1111 susceptibility of clouds to aerosol perturbations, *Geophys. Res. Lett.*, 36,
1112 <https://doi.org/10.1029/2009GL038993>, 2009.

1113 Terai, C. R. and Wood, R.: Aircraft observations of cold pools under marine stratocumulus, *Atmos.*
1114 *Chem. Phys.*, 13, 9899-9914, 10.5194/acp-13-9899-2013, 2013.

1115 Terai, C. R., Wood, R., Leon, D. C., and Zuidema, P.: Does precipitation susceptibility vary with
1116 increasing cloud thickness in marine stratocumulus?, *Atmos. Chem. Phys.*, 12, 4567-4583,
1117 10.5194/acp-12-4567-2012, 2012.

1118 Twohy, C. H., Petters, M. D., Snider, J. R., Stevens, B., Tahnk, W., Wetzel, M., Russell, L., and Burnet,
1119 F.: Evaluation of the aerosol indirect effect in marine stratocumulus clouds: Droplet number, size,
1120 liquid water path, and radiative impact, *J. Geophys. Res.-Atmos.*, 110,
1121 <https://doi.org/10.1029/2004JD005116>, 2005.

1122 vanZanten, M. C., Stevens, B., Vali, G., and Lenschow, D. H.: Observations of Drizzle in Nocturnal
1123 Marine Stratocumulus, *J. Atmos. Sci.*, 62, 88-106, <https://doi.org/10.1175/JAS-3355.1>, 2005.

1124 Waławczyk, M., Ma, Y. F., Kopeć, J. M., and Malinowski, S. P.: Novel approaches to estimating the
1125 turbulent kinetic energy dissipation rate from low- and moderate-resolution velocity fluctuation
1126 time series, *Atmos. Meas. Tech.*, 10, 4573-4585, 10.5194/amt-10-4573-2017, 2017.

1127 Wang, J., Wood, R., Jensen, M. P., Chiu, J. C., Liu, Y., Lamer, K., Desai, N., Giangrande, S. E., Knopf,
1128 D. A., Kollias, P., Laskin, A., Liu, X., Lu, C., Mechem, D., Mei, F., Starzec, M., Tomlinson, J.,
1129 Wang, Y., Yum, S. S., Zheng, G., Aiken, A. C., Azevedo, E. B., Blanchard, Y., China, S., Dong,
1130 X., Gallo, F., Gao, S., Ghate, V. P., Glienke, S., Goldberger, L., Hardin, J. C., Kuang, C., Luke, E.
1131 P., Matthews, A. A., Miller, M. A., Moffet, R., Pekour, M., Schmid, B., Sedlacek, A. J., Shaw, R.
1132 A., Shilling, J. E., Sullivan, A., Suski, K., Veghte, D. P., Weber, R., Wyant, M., Yeom, J.,
1133 Zawadowicz, M., and Zhang, Z.: Aerosol and Cloud Experiments in the Eastern North Atlantic
1134 (ACE-ENA), *B. Am. Meteorol. Soc.*, 103, E619-E641, 10.1175/BAMS-D-19-0220.1, 2022.

1135 Wang, Y., Zhao, C., McFarquhar, G. M., Wu, W., Reeves, M., and Li, J.: Dispersion of Droplet Size
1136 Distributions in Supercooled Non-precipitating Stratocumulus from Aircraft Observations Obtained

1137 during the Southern Ocean Cloud Radiation Aerosol Transport Experimental Study, *J. Geophys.*
1138 *Res.-Atmos.*, 126, e2020JD033720, <https://doi.org/10.1029/2020JD033720>, 2021a.

1139 Wang, Y., Zheng, G., Jensen, M. P., Knopf, D. A., Laskin, A., Matthews, A. A., Mechem, D., Mei, F.,
1140 Moffet, R., Sedlacek, A. J., Shilling, J. E., Springston, S., Sullivan, A., Tomlinson, J., Veghte, D.,
1141 Weber, R., Wood, R., Zawadowicz, M. A., and Wang, J.: Vertical profiles of trace gas and aerosol
1142 properties over the eastern North Atlantic: variations with season and synoptic condition, *Atmos.*
1143 *Chem. Phys.*, 21, 11079-11098, 10.5194/acp-21-11079-2021, 2021b.

1144 Wang, Y., Zheng, X., Dong, X., Xi, B., Wu, P., Logan, T., and Yung, Y. L.: Impacts of long-range
1145 transport of aerosols on marine-boundary-layer clouds in the eastern North Atlantic, *Atmos. Chem.*
1146 *Phys.*, 20, 14741-14755, 10.5194/acp-20-14741-2020, 2020.

1147 Wang, Y., Zheng, X., Dong, X., Xi, B., and Yung, Y. L.: Insights of warm-cloud biases in Community
1148 Atmospheric Model 5 and 6 from the single-column modeling framework and Aerosol and Cloud
1149 Experiments in the Eastern North Atlantic (ACE-ENA) observations, *Atmos. Chem. Phys.*, 23,
1150 8591-8605, 10.5194/acp-23-8591-2023, 2023.

1151 Wallace, J. M. and Hobbs, P. V.: *Atmospheric Science: An Introductory Survey*, 2nd edn., Academic
1152 Press/Elsevier, 483 pp, 2006.

1153 Witte, M. K., Chuang, P. Y., Ayala, O., Wang, L.-P., and Feingold, G.: Comparison of Observed and Simulated
1154 Drop Size Distributions from Large-Eddy Simulations with Bin Microphysics, *Mon. Weather Rev.*, 147, 477-
1155 493, <https://doi.org/10.1175/MWR-D-18-0242.1>, 2019.

1156 Wood, R.: Drizzle in Stratiform Boundary Layer Clouds. Part I: Vertical and Horizontal Structure, *J.*
1157 *Atmos. Sci.*, 62, 3011-3033, 10.1175/JAS3529.1, 2005.

1158 Wood, R.: Rate of loss of cloud droplets by coalescence in warm clouds, *J. Geophys. Res.-Atmos.*, 111,
1159 <https://doi.org/10.1029/2006JD007553>, 2006.

1160 Wood, R., Wyant, M., Bretherton, C. S., Rémillard, J., Kollias, P., Fletcher, J., Stemmler, J., de Szoeki,
1161 S., Yuter, S., Miller, M., Mechem, D., Tselioudis, G., Chiu, J. C., Mann, J. A. L., O'Connor, E. J.,

1162 Hogan, R. J., Dong, X., Miller, M., Ghate, V., Jefferson, A., Min, Q., Minnis, P., Palikonda, R.,
1163 Albrecht, B., Luke, E., Hannay, C., and Lin, Y.: Clouds, Aerosols, and Precipitation in the Marine
1164 Boundary Layer: An Arm Mobile Facility Deployment, *B. Am. Meteorol. Soc.*, 96, 419-440,
1165 10.1175/BAMS-D-13-00180.1, 2015.

1166 Wu, P., Dong, X., and Xi, B.: A Climatology of Marine Boundary Layer Cloud and Drizzle Properties
1167 Derived from Ground-Based Observations over the Azores, *J. Climate*, 33, 10133-10148,
1168 10.1175/JCLI-D-20-0272.1, 2020.

1169 Wu, P., Dong, X., Xi, B., Liu, Y., Thieman, M., and Minnis, P.: Effects of environment forcing on marine
1170 boundary layer cloud-drizzle processes, *J. Geophys. Res.-Atmos.*, 122, 4463-4478,
1171 <https://doi.org/10.1002/2016JD026326>, 2017.

1172 Wyant, M. C., Bretherton, C. S., Wood, R., Blossey, P. N., and McCoy, I. L.: High Free-Tropospheric
1173 Aitken-Mode Aerosol Concentrations Buffer Cloud Droplet Concentrations in Large-Eddy
1174 Simulations of Precipitating Stratocumulus, *Journal of Advances in Modeling Earth Systems*, 14,
1175 e2021MS002930, <https://doi.org/10.1029/2021MS002930>, 2022.

1176 Yeom, J. M., Yum, S. S., Shaw, R. A., La, I., Wang, J., Lu, C., Liu, Y., Mei, F., Schmid, B., and
1177 Matthews, A.: Vertical Variations of Cloud Microphysical Relationships in Marine Stratocumulus
1178 Clouds Observed During the ACE-ENA Campaign, *J. Geophys. Res.-Atmos.*, 126,
1179 e2021JD034700, <https://doi.org/10.1029/2021JD034700>, 2021.

1180 Zawadowicz, M. A., Suski, K., Liu, J., Pekour, M., Fast, J., Mei, F., Sedlacek, A. J., Springston, S.,
1181 Wang, Y., Zaveri, R. A., Wood, R., Wang, J., and Shilling, J. E.: Aircraft measurements of aerosol
1182 and trace gas chemistry in the eastern North Atlantic, *Atmos. Chem. Phys.*, 21, 7983-8002,
1183 10.5194/acp-21-7983-2021, 2021.

1184 Zhang, J., Zhou, X., Goren, T., and Feingold, G.: Albedo susceptibility of northeastern Pacific
1185 stratocumulus: the role of covarying meteorological conditions, *Atmos. Chem. Phys.*, 22, 861-880,
1186 10.5194/acp-22-861-2022, 2022.

1187 Zhang, X., Dong, X., Xi, B., and Zheng, X.: Aerosol Properties and Their Influences on Marine Boundary
1188 Layer Cloud Condensation Nuclei over the Southern Ocean, *Atmosphere-Basel*, 14,
1189 10.3390/atmos14081246, 2023.

1190 Zheng, G., Wang, Y., Aiken, A. C., Gallo, F., Jensen, M. P., Kollias, P., Kuang, C., Luke, E., Springston,
1191 S., Uin, J., Wood, R., and Wang, J.: Marine boundary layer aerosol in the eastern North Atlantic:
1192 seasonal variations and key controlling processes, *Atmos. Chem. Phys.*, 18, 17615-17635,
1193 10.5194/acp-18-17615-2018, 2018.

1194 Zheng, G., Wang, Y., Wood, R., Jensen, M. P., Kuang, C., McCoy, I. L., Matthews, A., Mei, F.,
1195 Tomlinson, J. M., Shilling, J. E., Zawadowicz, M. A., Crosbie, E., Moore, R., Ziemba, L., Andreae,
1196 M. O., and Wang, J.: New particle formation in the remote marine boundary layer, *Nature*
1197 *Communications*, 12, 527, 10.1038/s41467-020-20773-1, 2021.

1198 Zheng, X., Dong, X., Ward, D. M., Xi, B., Wu, P., and Wang, Y.: Aerosol-Cloud-Precipitation
1199 Interactions in a Closed-cell and Non-homogenous MBL Stratocumulus Cloud, *Adv. Atmos. Sci.*,
1200 39, 2107-2123, 10.1007/s00376-022-2013-6, 2022a.

1201 Zheng, X., Xi, B., Dong, X., Wu, P., Logan, T., and Wang, Y.: Environmental effects on aerosol–cloud
1202 interaction in non-precipitating marine boundary layer (MBL) clouds over the eastern North
1203 Atlantic, *Atmos. Chem. Phys.*, 22, 335-354, 10.5194/acp-22-335-2022, 2022b.

1204 Zuidema, P., Torri, G., Muller, C., and Chandra, A.: A Survey of Precipitation-Induced Atmospheric
1205 Cold Pools over Oceans and Their Interactions with the Larger-Scale Environment, *Surveys in*
1206 *Geophysics*, 38, 1283-1305, 10.1007/s10712-017-9447-x, 2017.

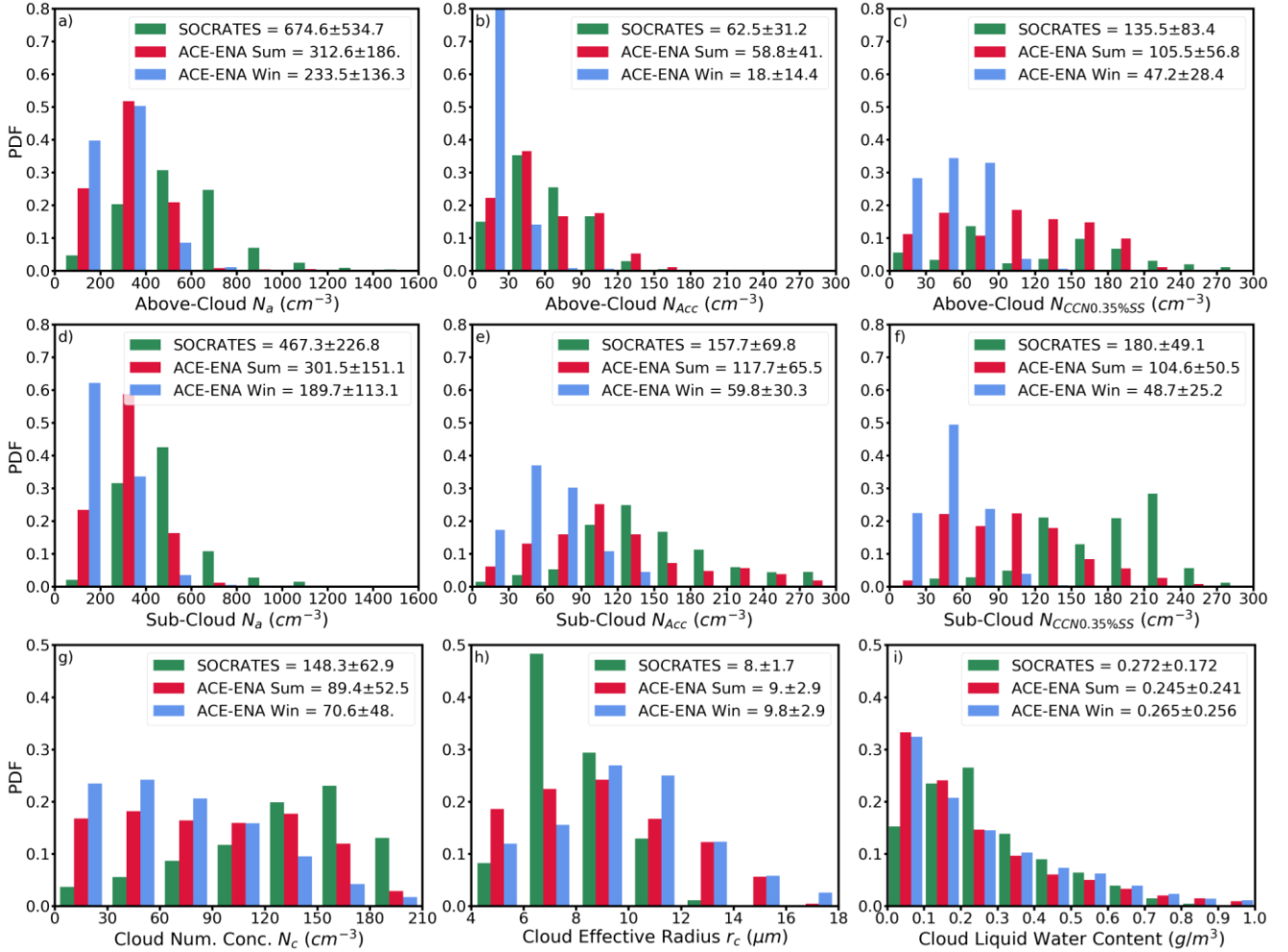


Figure 1. Probability Density Functions (PDFs) of N_a , N_{ACC} and $N_{CCN0.35\%}$ in the above-cloud (a, b, c) and sub-cloud (d, e, f) regimes; and the cloud microphysical properties of N_c (g), r_c (h), and LWC_c (f) within cloud layer. The statistical metrics in the legends denote the mean and standard deviation values for all samples in three IOPs. The ACE-ENA summer, winter and SOCRATES are color-coded with red, blue and green, respectively.

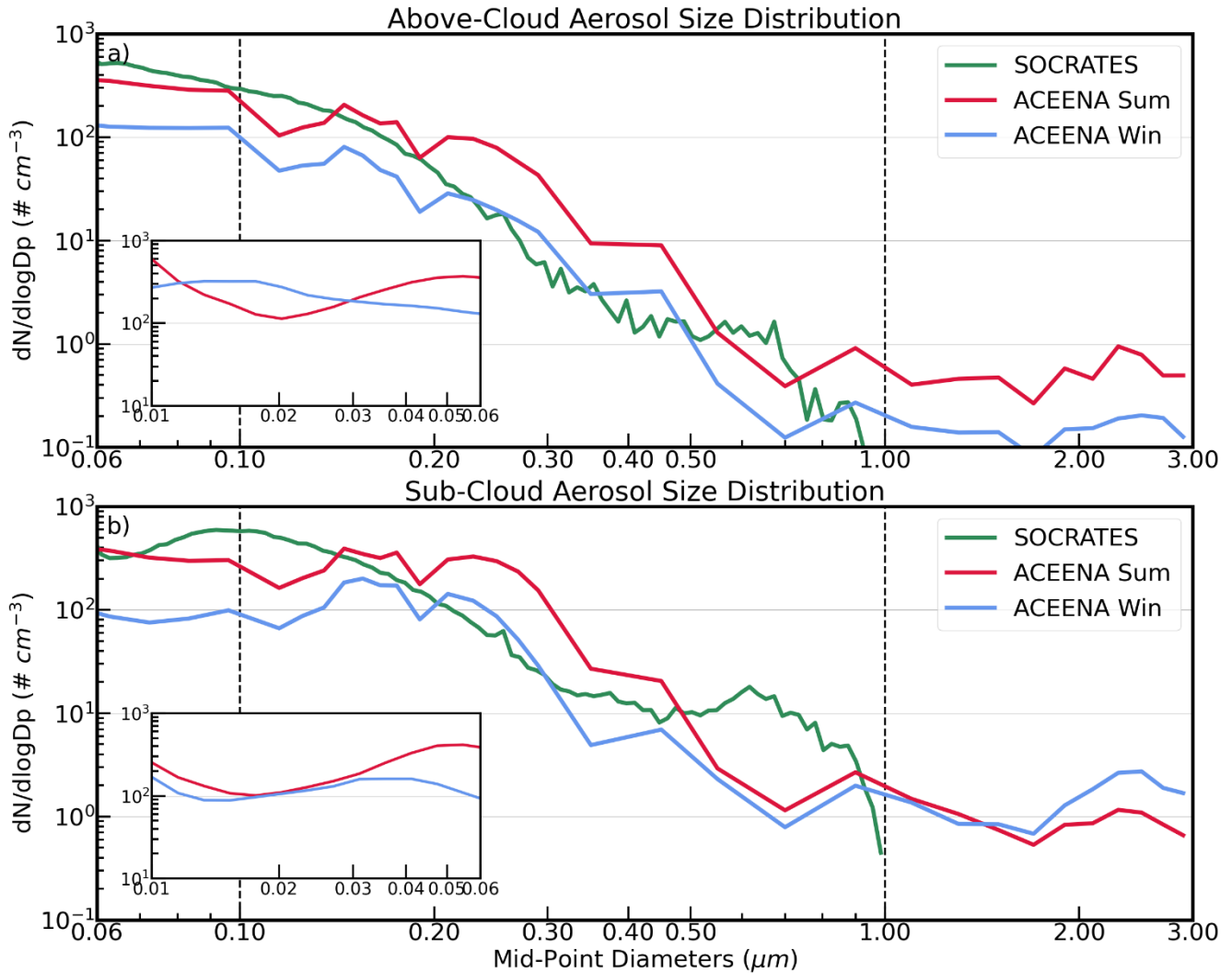
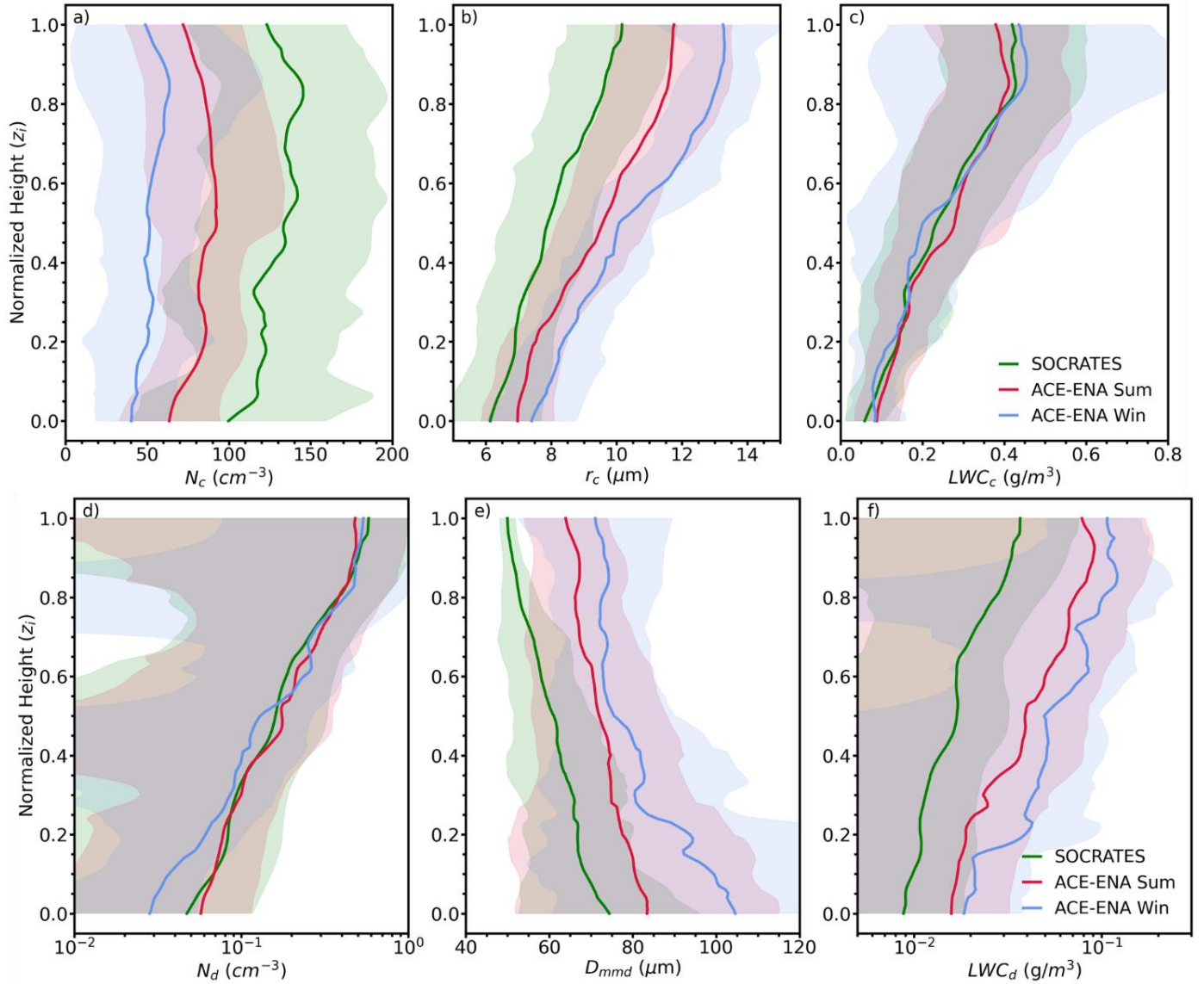
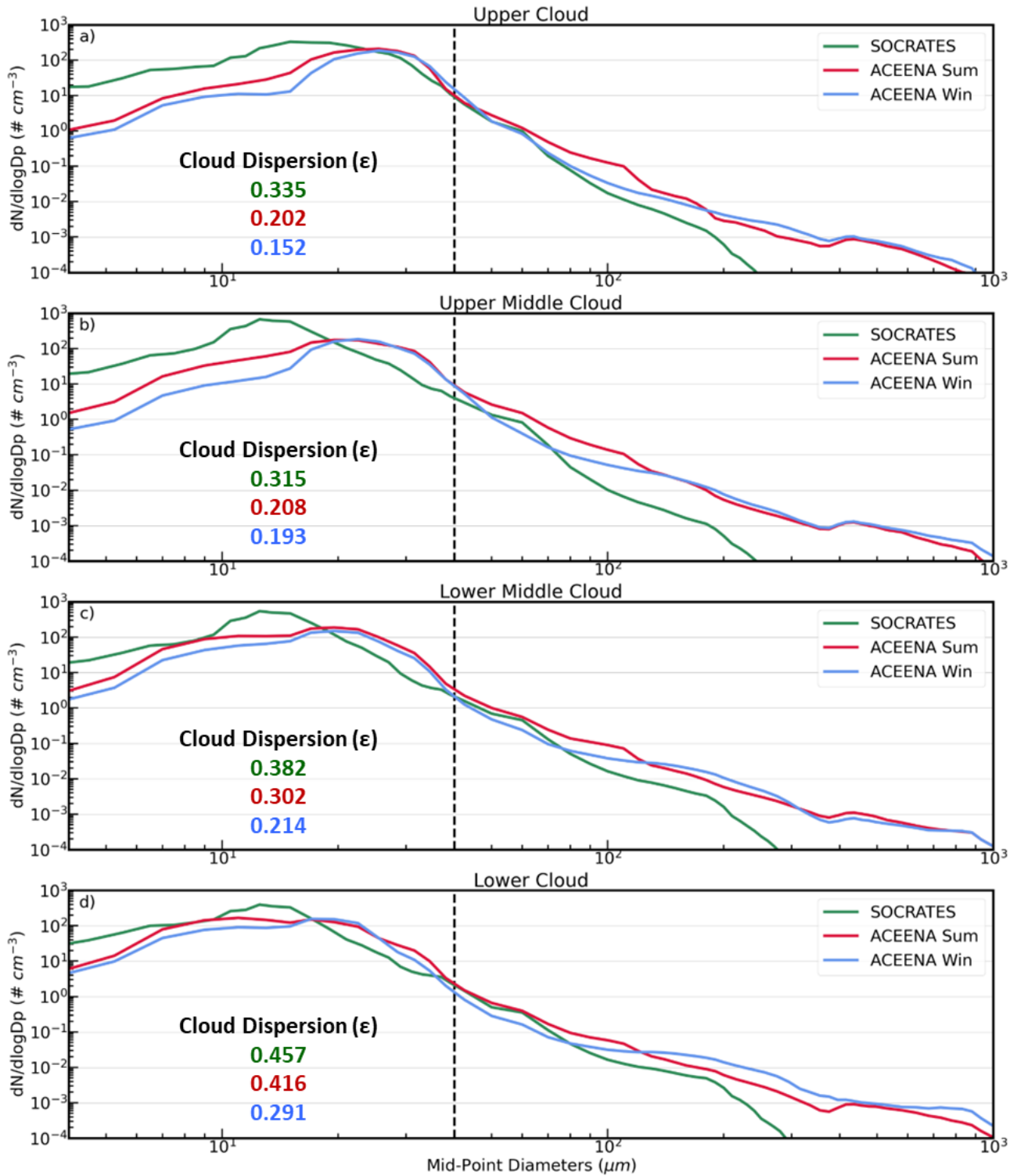


Figure 2. Aerosol size distributions ($D_p = 0.06 - 3 \mu\text{m}$) for above-cloud (a) and sub-cloud (b) regimes. The vertical dashed line at $D_p = 0.1 \mu\text{m}$ and at $D_p = 1 \mu\text{m}$ denotes the demarcations between Accumulation mode, Aitken mode and Coarse mode aerosols. The inner plots denote a smaller range of Aitken mode size distribution ($D_p = 0.01 - 0.06 \mu\text{m}$) available from ACE-ENA. The ACE-ENA summer, winter and SOCRATES are color-coded with red, blue and green, respectively.



1207 **Figure 3.** Vertical distributions of N_c (a), r_c (b), LWC_c (c), N_d (d), D_{mmd} (e), and LWC_d (f). Here the
 1208 $z_i = 0$ denotes cloud base and $z_i = 1$ denotes cloud top. Shaded areas denote the inter-cloud-case
 1209 standard deviations. The ACE-ENA summer, winter and SOCRATES are color-coded with red, blue and
 1210 green, respectively.



1211 **Figure 4.** Cloud and drizzle size distributions for a) upper cloud ($z_i > 0.8$), b) upper-middle cloud ($0.5 \leq$
 1212 $z_i < 0.8$), c) lower-middle cloud ($0.2 \leq z_i < 0.5$) and d) lower cloud ($z_i < 0.2$). The vertical dashed
 1213 line at $D_p = 40 \mu\text{m}$ denotes the demarcation between cloud droplets and drizzle drops. The ACE-ENA
 1214 summer, winter and SOCRATES are color-coded with red, blue and green, respectively.

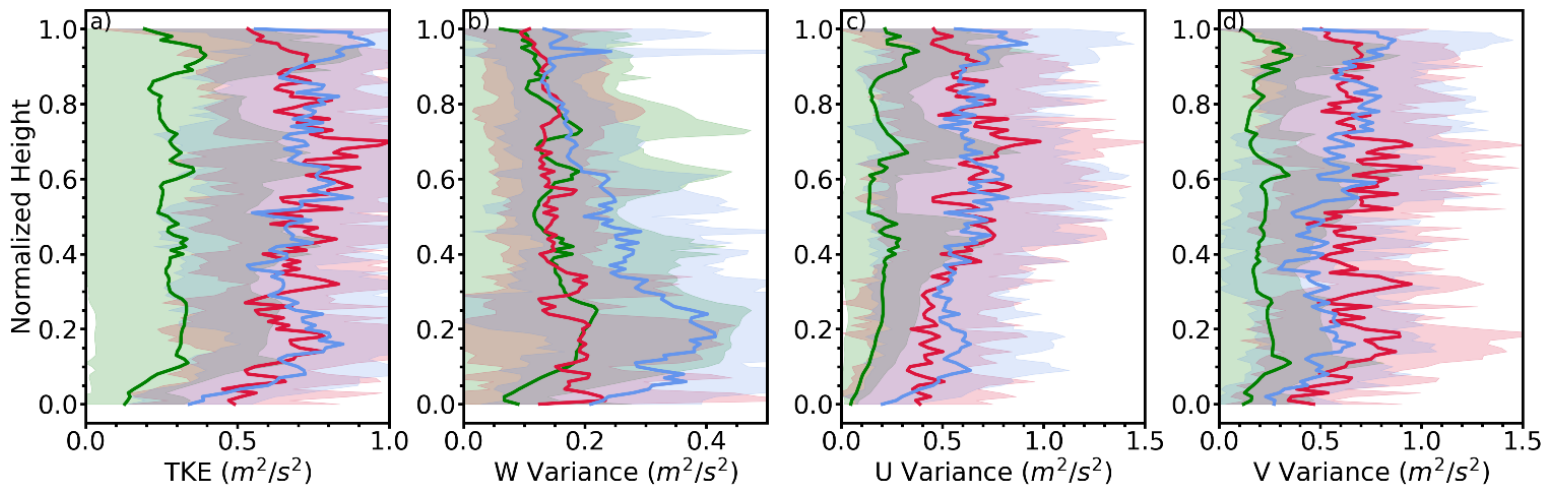


Figure 5. Vertical distributions of in-cloud TKE (a), w'^2 (b), u'^2 (c) and v'^2 (d). Shaded areas denote the inter-cloud-case standard deviations. The ACE-ENA summer, winter and SOCRATES are color-coded with red, blue and green, respectively.

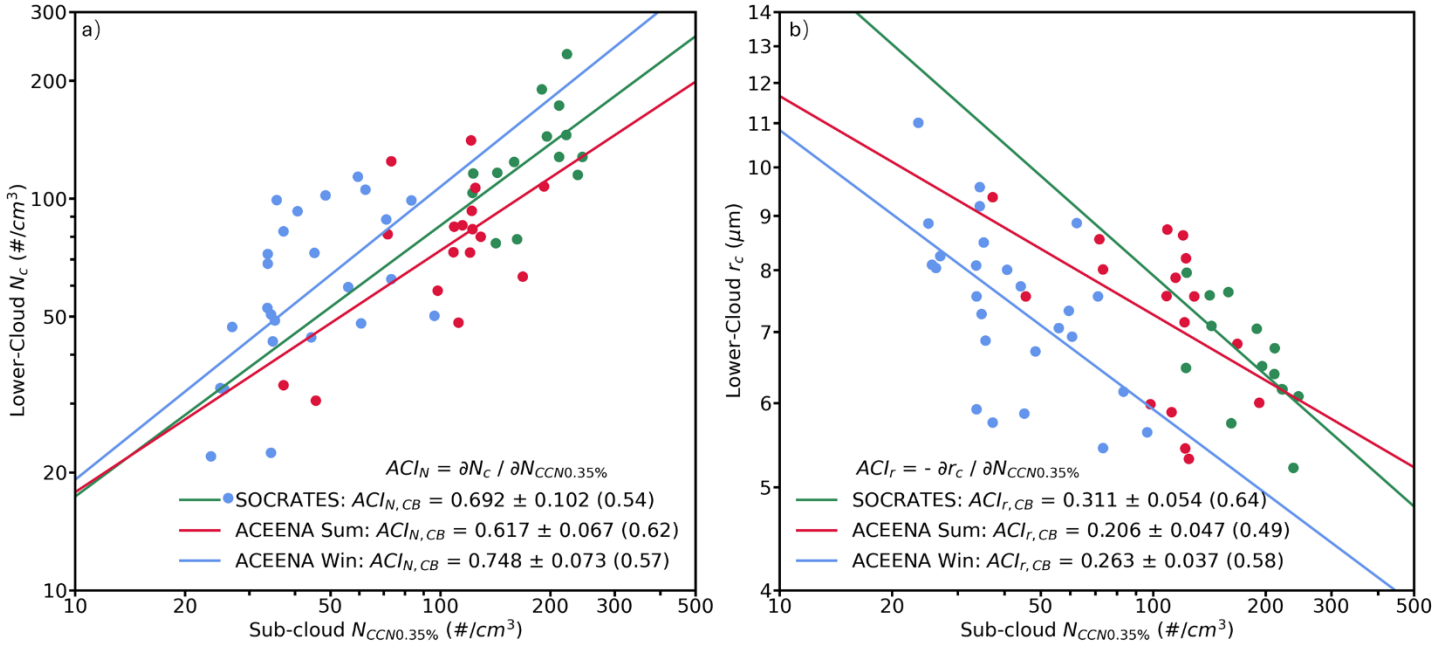


Figure 6. Scatterplots of the a) N_c and b) r_c at the lower-cloud ($z_i < 0.2$) against the sub-cloud $N_{CCN0.35\%}$. The statistical metrics in the legends denote the ACI values and standard errors, and the absolute values of correlation coefficients (in parentheses). The ACE-ENA summer, winter and SOCRATES are color-coded with red, blue and green, respectively.

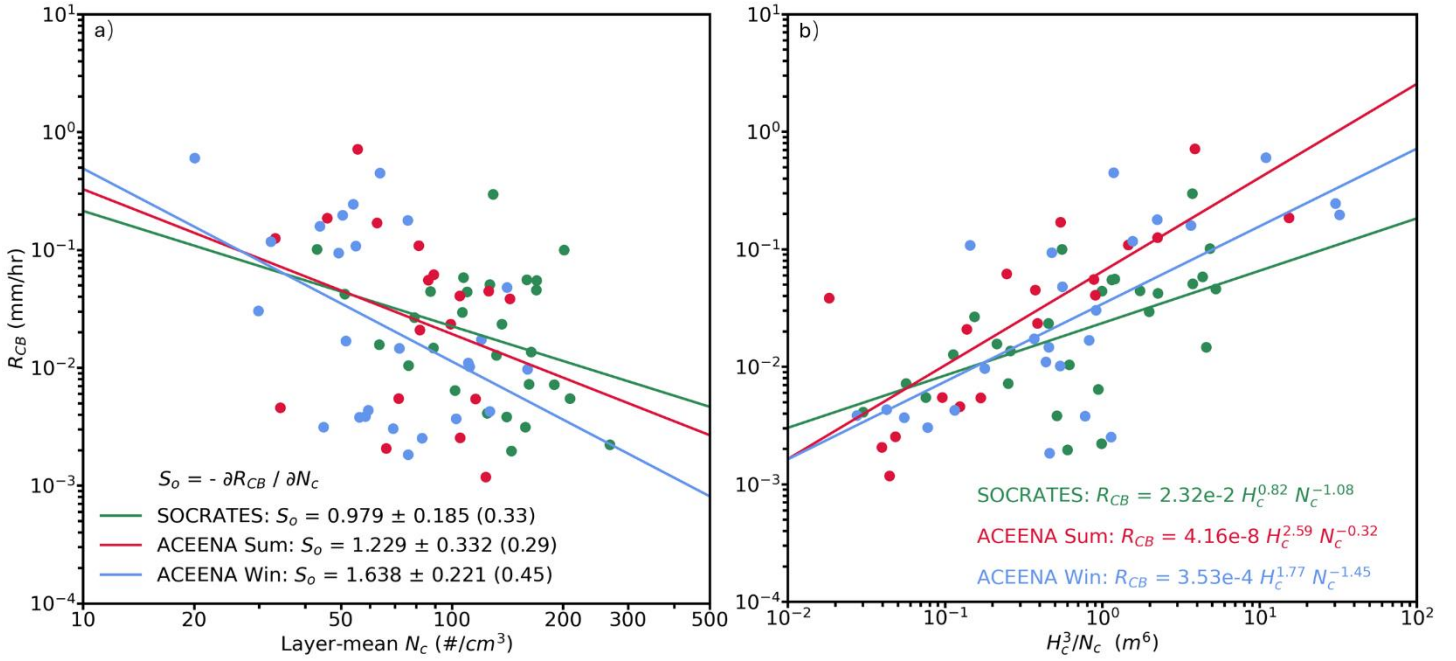


Figure 7. Scatterplots of the cloud base precipitation rate R_{CB} against the a) layer-mean N_c and b) H_c^3/N_c . ACE-ENA summer, winter and SOCRATES are color-coded with red, blue and green, respectively.

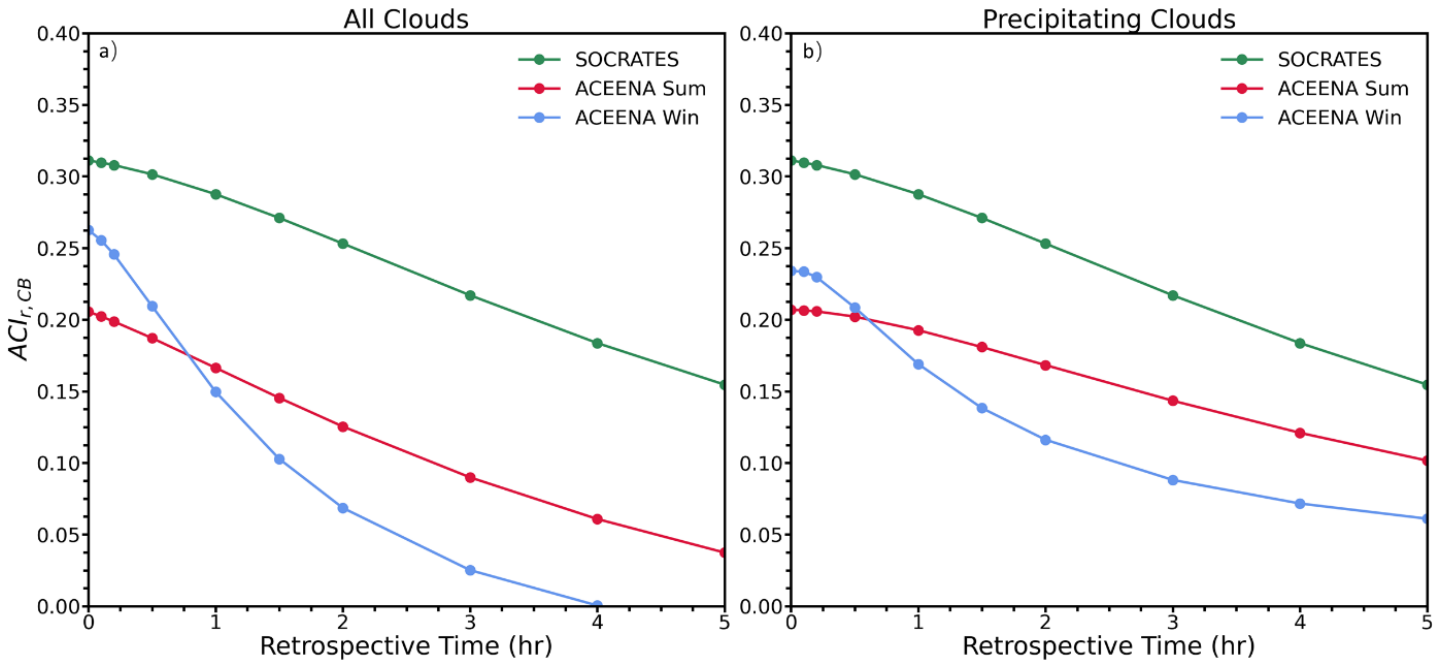


Figure 8. $ACI_{r,CB}$ as a function of the sub-cloud $N_{CCN0.35\%}$ retrospective time for a) all clouds and b) precipitating clouds.